

Summer 8-12-2015

Dynamic Characteristics of Biologically Inspired Hair Receptors for Unmanned Aerial Vehicles

Manohar Chidurala
mchidura@uno.edu

Follow this and additional works at: <https://scholarworks.uno.edu/td>



Part of the [Aerodynamics and Fluid Mechanics Commons](#), and the [Dynamics and Dynamical Systems Commons](#)

Recommended Citation

Chidurala, Manohar, "Dynamic Characteristics of Biologically Inspired Hair Receptors for Unmanned Aerial Vehicles" (2015). *University of New Orleans Theses and Dissertations*. 2040.
<https://scholarworks.uno.edu/td/2040>

This Dissertation is protected by copyright and/or related rights. It has been brought to you by ScholarWorks@UNO with permission from the rights-holder(s). You are free to use this Dissertation in any way that is permitted by the copyright and related rights legislation that applies to your use. For other uses you need to obtain permission from the rights-holder(s) directly, unless additional rights are indicated by a Creative Commons license in the record and/or on the work itself.

This Dissertation has been accepted for inclusion in University of New Orleans Theses and Dissertations by an authorized administrator of ScholarWorks@UNO. For more information, please contact scholarworks@uno.edu.

Dynamic Characteristics of Biologically Inspired Hair Receptors for Unmanned Aerial Vehicles

A Dissertation

Submitted to the Graduate Faculty of the
University of New Orleans
in partial fulfillment of the
requirements for the degree of

Doctor of Philosophy
in
Engineering and Applied Science
Mechanical Engineering

by

Manohar Chidurala

B.Tech. Jawaharlal Nehru Technological University, 2006
M.S. University of New Orleans, 2009

August, 2015

Copyright 2015, Manohar Chidurala

To my Parents

Acknowledgment

I would like to attribute the success of this dissertation project to Dr. Uttam K. Chakravarty, Assistant Professor of Mechanical Engineering. Dr. Chakravarty with his strong intellect and motivating personality inculcated a positive attitude in me. The present dissertation would not have been possible without his elaborate guidance and full encouragement. I would also like to thank Dr. Carsie A. Hall, Associate Professor of Mechanical Engineering, for his esteemed guidance and help throughout my graduate studies.

I would like to express my sincere thanks to Dr. George E. Ioup, Professor of Physics, and Dr. Ralph A. Saxton, Professor of Mathematics for serving on my dissertation committee and their help in courses and projects. I would like to thank Dr. Paul, J. Schilling, Chair of Mechanical Engineering Department, Dr. Paul D. Herrington, Professor of Mechanical Engineering and Dr. Martin J. Guillot, Associate Professor and graduate coordinator of Mechanical Engineering, for readily accepting to serve on my dissertation committee. I would also like to thank the Department of Mechanical Engineering at the University of New Orleans for providing financial assistance during my studies.

I am extremely grateful to my colleagues Jose Rubio, Pratik Sarker and Shafiqur Rahman for their encouragement and support.

I feel indebted to my family for their never ending support and encouragement. I would like to thank especially to my wife Ambika, my brother Srinivas and my Parents, without them, this part of journey would be inevitable.

Table of Contents

Nomenclature	vii
List of Figures	ix
List of Tables	xii
Abstract	xiii
1. Introduction.....	1
1.1. Biomimetic Artificial Hair Sensors and Applications	2
1.2. Numerical Modeling	6
1.3. Euler-Bernoulli Beam Theory.....	8
1.4. Natural Frequency and Mode Shapes	10
1.5. Computational Modeling	11
1.6. Multiple Hair Sensors	13
2. Natural Frequency and Mode Shapes of the Hair Receptor	15
2.1. Assumptions.....	15
2.2. Euler-Bernoulli Equation of Motion of Hair Receptor	16
2.3. Natural Frequencies of a Hair Receptor.....	20
2.4. Mode Shapes of a Hair Receptor	23
3. Fluid-Structure Interaction.....	25
3.1. CFD Model	26
3.1.1. Single Hair Receptor Model	26
3.1.2. Multiple Hair Receptors Model	27
3.1.3. Fluid Properties.....	28
3.1.4. Mesh Generation.....	28
3.1.5. Boundary Conditions on the Fluid.....	31
3.1.6. Boundary Conditions on the Mesh	31
3.2. Structural Model	33
3.2.1. Single Hair Receptor Model	33
3.2.2. Multiple Hair Receptors Model	33

3.2.3. Structural Properties.....	34
3.2.4. Mesh Generation.....	35
3.2.5. Boundary Conditions on the Hair Receptor.....	36
3.3. Fluid-Structure Interaction Analysis.....	37
3.4. Solution Procedure.....	39
4. Validation of Results.....	42
4.1. Validation of Structural Model.....	42
4.1.1. Mode Shapes of Hair Receptors.....	44
4.2. Mesh Independence Study for FSI Simulation.....	44
4.3. Experimental Validation.....	46
5. Results and Discussion.....	51
5.1. Single Hair Receptor Study.....	51
5.2. Multiple Hair Receptors Study.....	60
6. Conclusions.....	63
References.....	66
Vita.....	74

Nomenclature

d	Diameter of hair receptor
l	Length of hair receptor
A_s	Cross-sectional area of hair receptor
ρ	Density of air
ρ_s	Density of hair
E	Elastic modulus of the hair
I	Moment of inertia
ν	Poisson's ration
μ	Dynamic viscosity of air
w	Deflection of the hair receptor
P_∞	Atmospheric pressure
P	Pressure
V_∞	Freestream velocity magnitude
V	Velocity magnitude of fluid
\bar{V}	Average velocity of fluid
U	Displacement
UR	Rotation
u	Nodal displacement vector
M_s	Structural mass matrix
K_s	Structural stiffness matrix
D_s	Structural damping matrix

L_s	Applied load vector
ω	Natural frequencies of the hair receptor
∇	Gradient symbol
\vec{V}	Flow velocity vector
$\vec{\tau}$	Deviatoric stress tensor
\vec{f}	Body forces per unit volume
t	Time increment
n	Index for number of iterations
x	Spatial increment in the x-direction
y	Spatial increment in the y-direction
z	Spatial increment in the z-direction

List of Figures

- Figure 1 A clamped-free cylindrical (beam) hair receptor
- Figure 2 Plot of the first three mode shapes of the clamped-free hair structure
- Figure 3 Computational domain for flow around a hair receptor
- Figure 4 Computational domain for flow around multiple hair receptors
- Figure 5 Computational meshing of the fluid domain with a single hair receptor
- Figure 6 Computational meshing of the fluid domain with multiple hair receptors
- Figure 7 Meshing on the surface of the cylinder in fluid domain
- Figure 8 Computational domain of a single hair receptor
- Figure 9 Computational domain of multiple hair receptors
- Figure 10 The mesh generated for the hair receptor
- Figure 11 The mesh generated for multiple hair receptors
- Figure 12 Illustration of fluid-structure co-simulation boundary in the fluid domain
- Figure 13 Illustration of fluid-structure co-simulation boundary in the structural domain
- Figure 14 The variations of the first three natural frequencies of the hair receptor in a vacuum
- Figure 15 First, second, and third mode shapes of the hair receptor in a vacuum
- Figure 16 Mesh independence study for CFD model by monitoring the velocities at the tip of the hair receptor inside the fluid domain
- Figure 17 Model geometry for flow around the cylinder
- Figure 18 C_p distributions around the upper part of the cylinder surface
- Figure 19 Velocity contours for flow around the cylinder
- Figure 20 Velocity vectors for flow around the cylinder

- Figure 21 Pressure contours for flow around the cylinder
- Figure 22 Time-varying deflections of the flexible hair receptor at the tip
- Figure 23 Time-varying velocity magnitudes of the flexible hair receptor at the tip
- Figure 24 Deflection contour plot of the flexible hair receptor at the time of 0.25 seconds in steady flow
- Figure 25 Deflection contour plot of the flexible hair receptor at the time of 0.50 seconds in steady flow
- Figure 26 Deflection contour plot of the flexible hair receptor at the time of 0.75 seconds in steady flow
- Figure 27 Deflection contour plot of the flexible hair receptor at the time of 1.0 seconds in steady flow
- Figure 28 Deflection contour plot of the flexible hair receptor at the time of 0.25 seconds in unsteady flow
- Figure 29 Deflection contour plot of the flexible hair receptor at the time of 0.50 seconds in unsteady flow
- Figure 30 Deflection contour plot of the flexible hair receptor at the time of 0.75 seconds in unsteady flow
- Figure 31 Deflection contour plot of the flexible hair receptor at the time of 1.0 seconds in unsteady flow
- Figure 32 Velocity contour plot of the flexible hair receptor at the time of 1.0 seconds in steady flow
- Figure 33 Velocity contour plot of the flexible hair receptor at the time of 1.0 seconds in unsteady flow
- Figure 34 Pressure contour plot of the flexible hair receptor at the time of 1.0 seconds in steady flow
- Figure 35 Pressure contour plot of the flexible hair receptor at the time of 1.0 seconds in unsteady flow
- Figure 36 Deflection contour plot of the multiple hair receptors in steady flow
- Figure 37 Velocity contour plot of the multiple hair receptors in steady flow

Figure 38 Pressure contour plot of the multiple hair receptors in steady flow

List of Tables

Table 1	The first three eigenvalues of cantilever hair receptor model
Table 2	Material properties for the CFD model
Table 3	Boundary conditions for the CFD model
Table 4	Materials properties of the structural model
Table 5	Boundary conditions for the structural model
Table 6	Comparison of natural frequencies of the hair receptor in a vacuum between FE model and analytical model

Abstract

The highly optimized performance of nature's creations and biological assemblies has inspired the development of their engineered counter parts that can potentially outperform conventional systems. In particular, bat wings are populated with air flow hair receptors which feedback the information about airflow over their surfaces for enhanced stability and maneuverability during their flight. The hairs in the bat wing membrane play a role in the maneuverability tasks, especially during low-speed flight. The developments of artificial hair sensors (AHS) are inspired by biological hair cells in aerodynamic feedback control designs. Current mathematical models for hair receptors are limited by strict simplifying assumptions of creeping flow hair Reynolds number on AHS fluid-structure interaction (FSI), which may be violated for hair structures integrated on small-scaled Unmanned Aerial Vehicles (UAVs). This study motivates by an outstanding need to understand the dynamic response of hair receptors in flow regimes relevant to bat-scaled UAVs. The dynamic response of the hair receptor within the creeping flow environment is investigated at distinct freestream velocities to extend the applicability of AHS to a wider range of low Reynolds number platforms. Therefore, a three-dimensional FSI model coupled with a finite element model using the computational fluid dynamics (CFD) is developed for a hair-structure and multiple hair-structures in the airflow. The Navier-Stokes equations including continuity equation are solved numerically for the CFD model. The grid independence of the FSI solution is studied from the simulations of the hair-structure mesh and flow mesh around the hair sensor. To describe the dynamic response of the hair receptors, the natural frequencies and mode shapes of the hair receptors, computed from the finite element model, are compared with the excitation frequencies in vacuum. This model is described with both the boundary layer effects and effects of inertial forces due to fluid-structure

interaction of the hair receptors. For supporting the FSI model, the dynamic response of the hair receptor is also validated considering the Euler-Bernoulli beam theory including the steady and unsteady airflow.

Keywords: Biomimetic Artificial Hair Sensors, Fluid-Structure Interactions, Euler-Bernoulli Beam Theory, Unmanned Aerial Vehicles (UAVs), and Creeping Flow

Chapter 1

Introduction

Many animals receive the information from their hair-like receptors to detect prey or to enhance the locomotion that are surrounded by the fluid flows. Biomimetic flow sensors/receptors are still in their early stage of development. Further efforts are required to unveil the sensing mechanisms from the natural biological systems and to achieve the multi-level bio-mimicking of the natural system through the development of their artificial counter parts. In particular, bats have airflow hair sensors on their dorsal and ventral wing surfaces which bend and twist and produce signals through the hair roots to the skin. This helps to avoid the stall of the wings and to increase the agility and maneuverability during their flight. The utility of biological hair receptors has motivated the development of artificial hair sensors (AHS) in aerodynamic feedback control design systems. GPS, inertia based accelerometers, hot wire, and barometers for fluid flow detection may not be good options for small-scaled unmanned aerial vehicles (UAVs) due to the weight concern. Therefore, the installation of the AHS on the leading edges of the wings of UAVs to improve the aerodynamic control is a possible solution. For such applications, the flow phenomena related to aerodynamic forces can be detected through the dynamic response of AHS must be understood.

The present study incorporates the fluid-structure interaction analysis of a hair receptor in flow regimes relevant to bat-scaled UAVs. In this work, the development of FSI models for single hair receptor and multiple hair receptors is presented. The present analysis is conducted within the creeping flow where Reynolds number is less than one. The three-dimensional FSI

model will be used to present the velocity, pressure, and deflection contour plots of multiple hair receptors in both steady and unsteady flow. This study investigates the possibility of installing multiple hair receptors thus the fluid-structure interaction in between them can be discussed.

The literature is divided into dynamic modeling of hair receptors under the action of fluid loading. It is focused on frequency response of cantilever beam type hair receptors oscillated by fluid flows. Many computational and numerical analyses of hair sensors vibrating in fluids have been reported in the literature. The interaction can take place due to fluid flow which can be normal to the neutral axis of a hair receptor.

1.1. Biomimetic Artificial Hair Sensors and Applications

The roles of the wing's hair of bats were studied by Sterbing-D'Angelo et al. [1] in which flight experiments were conducted that involved depilation of the hairs and the flight performance after depilation. Their results showed that the wing hair removal along the trailing edge alone statistically caused the same effects as the depilation of the entire wing. This biological understanding motivates engineering questions on the functions of artificial hair sensors for the navigation and control designs of small-scaled aircraft like unmanned air vehicles. They also quantified the directional sensitivity of the distributed hair receptors which suggested specialization of the hair array for the detection of reversed flow over the dorsal wing surface.

Dickenson et al. [2] studied the wing hair receptor arrays for airflow feedback in bats which inspired the use of AHS for micro air vehicles (MAVs). Similarly, flow sensitive hair arrays found on the bodies of fishes and implicated in their locomotions (Coombs [3] and Liu

[4]) inspired the application of AHS to underwater vehicles. In both engineering applications, low-Reynolds number regimes challenged vehicle stability, maneuverability or overall efficiency through unsteady aerodynamic or hydrodynamic forces. As low-Reynolds number animals (e.g. bats and fishes) could use hair receptors as part of a feedback control loop, AHS could play a similar role in low-Reynolds number vehicles. For bats, one means of control (actuation) is simply changing the shape or kinematics of its wings during flapping flight. According to the study conducted by Abdulrahim et al. [5], micro air vehicle actuators included in the typical aircraft control surfaces (ailerons, rudders, elevators and flaps) and wing morphing.

An overview of the wide range of biomimetic sensor technologies and their innovations were provided by Stroble et al. [6]. They also introduced the biomimetic sensors with their types, their advantages and how they were different from traditional sensors. Bat wing hair receptors were used for airflow feedback by Zook [7] and hair receptors were thought to be specialized for boundary layer detection. Chada et al. [8] detected the flow structure known as the leading edge vortex. Based on boundary layer fluctuations, bats could sense the state of the flow above their wings to enhance flight. Numerical studies showed by Dickenson et al. [9] and Dickenson [10] involved the mechanical response of hair arrays and provided a time and space accurate representation of boundary layer development and flow separation over a cylinder.

In a separate biological hair sensor study, Joshi et al. [11] studied the response of the socket structure in which the hair base sat and encompassed the hair below the skin of the cricket; the deformation and stress transfer applied in the design of a highly responsive MEMS sensor. The mathematical modeling of the motion of arthropod filiform hairs in oscillating air flows were carried out by Humphrey et al. [12]. In this study, numerical models were developed

to predict the qualitative aspects of known hair motion in response to air movement in which hair motion behavior was analyzed based on the numerical calculations of the equation for conservation of hair angular momentum where air oscillated both parallel and normal to the axis of the cylinder substrate supporting the hair.

Numerous active artificial hair sensors had also been developed. Tao et al. [13] provided a comprehensive review on bio-inspired hair flow sensors which included the basic sensing mechanisms in biological hair flow sensors and the achievements on biomimetic devices to date. Maschmann et al. [14] evaluated the comprehensive electromechanical response of aligned carbon nanotube (CNT) arrays used as an artificial hair sensor and demonstrated their high sensitivity, repeatability, and rapid response time. Yu et al. [15] developed a bio-inspired sensor for monitoring turbulent flow which consisted of an array of micro-pillars or nano-pillars. Chen et al. [16] characterized the performance of the AHC sensor under oscillatory water flow in addition to steady-state water flow and airflow. Tucker et al. [17] presented the highly sensitive flow-field measurements of AHC sensor for oscillating flow field down to 0.6 mm/s and steady state flow fields detected down to 0.1 mm/s.

Looking forward to applications of AHS on membrane wing structures, bat scale membrane wing research is briefly noted. Moliki and Breuer [18] investigated the deformation and oscillatory motion of a membrane at Reynolds numbers 38,416 and 141,500 for the applications involving the flight of micro air vehicles and the membrane wings of flying mammals such as bats. Rojratsirikul et al. [19] investigated the aerodynamic characteristics of two-dimensional membrane airfoil in a wind tunnel at low Reynolds numbers. Miao and Ho [20] investigated the effect of chord-wise flexure amplitude on unsteady aerodynamic characteristics

for a flapping airfoil under Reynolds numbers 10,000. Mueller and DeLaurier [21] described the effects of Reynolds number and aspect ratio on the design and performance of fixed-wing vehicles such as UAVs and also discussed the influence of laminar separation aeroelastic behavior of flapping wing. Mangalam and Moes [22] observed the critical surface, viscosity-related aerodynamic phenomena under both steady and unsteady flight conditions. Lee and Lee [23] presented a numerical scheme for fluid-structure interaction (FSI) for flexible plate in unsteady flows with Reynolds numbers up to 120 in which the Lattice Boltzmann method with an immersed boundary technique using a direct forcing scheme was used for the fluid and a finite element method with Euler beam elements was used for the flexible plate.

Many arthropods use filiform hairs as mechanoreceptors to detect air motion. Cummins et al. [24, 25] presented a model capable of calculating hair-to-hair coupling in arbitrary configurations in which they analyzed the viscosity-mediated coupling at low frequencies to investigate the interaction between arthropod filiform hairs in a fluid environment. They found that the coupling effects were non-negligible, and likely constrained the operational characteristics of the cercal sensory array. Kim et al. [26] presented a micro-machined circular type thermal flow sensor capable of the simultaneous detection of both the flow rate and the flow direction. Su et al. [27] developed a piezoresistive-type flow sensor with a silicon cantilever probe, in which the gas flow was measured by a strain gauge attached to the root of the cantilever beam.

Feathers are equipped with a variety of sensors which are able to detect both position and movements. There are hairs-like feathers associated with most feathers which play a special role as sensory "hairs". Interestingly the information of these sensors (Necker [28]) was transmitted

directly to the cerebellum of the brain which was very important for the control of locomotion. Behavioral evidence on the roles of various input sources was summarized by Haskell [29]. Sensory sensilla on the wing and other body parts of insects were showed by Pflueger et al. [30], to play a role in flight control, as have vibrotactile receptors at the feather base of birds. Cricket sensory hairs were highly sensitive to drag-forces exerted on the hair shaft. Dijkstra et al. [31] presented the modeling, design, fabrication, and characterization of flow sensors based on the wind-receptor hairs of crickets.

1.2. Numerical Modeling

To understand the mechanical response of hair structures, FSI studies are investigated passive cantilevers in various flow environments. Numerical studies for fluid-structure interaction analysis are involved the coupling of fluid and structure. The fluid flow is governed by momentum equation and continuity equation. This section is provided a brief literature on the numerical methods applied for solving fluid flow problems.

The optimal hair lengths for detecting changes in laminar boundary layer velocity profile agreed with the lengths of bat wing hair receptors were reported by Dickinson [32]. McClain et al. [33] studied the response of passive hair elements with aspect ratios representative of biological systems attached to surfaces interacting with steady boundary layers. The dynamic behavior of a nonlinear beam coupled with a potential flow was studied by Emamiya et al. [34]. In the aforementioned paper, suitable energy norms for analyzing the dynamics of the nonlinear beam by itself as well as for the fluid-beam coupled problems were developed and corresponding stability estimates were proved. Dickinson et al. [35] also proposed a nonlinear viscoelastic model of a hair-like structure coupled to an unsteady non-uniform flow environment and showed

how arrays of flexible hair-like structures provided a space and time accurate representation of near surface flow phenomena through simulations of a flexible hair array in a laminar unsteady flow separation over a cylinder.

When a structure is vibrating in a viscous fluid, the fluid exerts on it a load called hydrodynamic force. In case of small amplitude of vibration, Weiss et al. [36] and Tuck [37] found that the hydrodynamic force was a function of the amplitude of vibration. A lot of filiform hairs function as a sensory system for raider detections and communications in life. The hair was affected significantly by boundary-layer flows and was deflected by drag forces acting on the hair shaft. Shimozawa [38] concluded that it was high moment of inertia made irresponsive to high frequency air motion. Dechant [39] showed that the hair shaft could be deflected and bent by a direct contact. The dynamics of hair movement in an oscillating fluid had been modeled extensively [40-42] where the filiform hair was assumed as an inverted pendulum with a rigid shaft supported by a spring and a damper at the base.

Byung et al. [43] proposed the flexible beam model for the flow sensory hair to investigate the behavior of a flexible filiform hair where the forces acting on the hair were due to drag and virtual mass of the surrounding flow. In the latter study, the magnitudes of generalized coordinates were compared with their phase diagrams to understand the dynamics of an artificial hair-cell sensor. Hossain and Mian [44] investigated the dynamic response of a mini cantilever beam by changing the density and viscosity associated with different viscous fluids and then experimental results compared with the finite element analysis model for validation. Implications for biomimetic flow-sensing MEMS were presented by Steinmann et al. [45]. In their study, the boundary layers over small appendages in insects in longitudinal and transverse oscillatory flows

were characterized. Motion response of filiform hairs was compared to sinusoidal oscillations in air and in water by Devarakonda et al. [46]. Their results concluded that hairs in air were more sensitive to changes in hair length regarding resonance frequency whereas hairs in water were the more sensitive regarding the amplitude of motion.

1.3. Euler-Bernoulli Beam Theory

To investigate the tip deflections of the artificial hair receptors in the laminar boundary layer flow, each hair is modeled with an Euler-Bernoulli beam equation coupled to the flow with solution data from the Navier-Stokes equations. A brief literature review related to the applications of Euler-Bernoulli beam theory is provided in this section.

The maximum hair tip deflection was assumed to be less than 10% of its length in the analysis studied by Dickenson et al. [32]. This ensured that despite hair bending, a small angle approximation to the velocity profile incident normal to the undeflected hair was valid. To test this assumption, they performed a finite element analysis of a static Euler–Bernoulli beam (similar to the work in [2]), 1.0 m from the leading edge of a plate subject to the Blasius boundary layer with external flow of 10 m/s, hair length equal to the boundary layer thickness, a diameter of 1% of its length (6.2×10^{-5} m) and modulus of elasticity of 2.0 GPa (representative of nylon). An Euler-Bernoulli beam approach was presented for modeling the deflection of non-orthogonal wall mounted parts. Dickinson [47] investigated the dynamic response of a carbon fiber filament in oscillatory boundary layer flows with quasi-steady nonlinear viscoelastic model to better understand their tendencies for vibration.

One of the main difficulties in simulating nonlinear structures in dynamic regime is to find an integrator sufficiently precise and stable for long simulation periods of time. In the work presented by Cao et al. [48, 49], a free cantilever beam was evaluated using Cosserat beam element obtained from third order approximation of shape functions. They used the Newmark scheme with imposed conservation of mechanical energy integration method suggested by Bathe [50]. Badiane et al. [51] presented a finite element model of an apparatus, based on the phenomenon of resonance, for measuring the viscosity of Newtonian fluids. The study was based on a cantilever beam in a viscous fluid excited by an electromagnetic force. The Bernoulli-Euler equation was used to model the beam and to linearize Navier-Stokes equations for the fluid and the Maxwell equations were used for the magnetic-structure interaction. The action of the fluid on the beam was modeled by hydrodynamic resistance coefficients. A semi numerical model of a vibrating beam was obtained and results were used to model the vibrating viscometer.

The vibrations of nonlinear beam structures have been a subject of great interest in the broad field of structural mechanics [52]. There were several classical approaches employed to solve the governing nonlinear differential equations to study the nonlinear vibrations including perturbation methods [53], form-function approximations [54], finite element methods [55] and hybrid approaches [56]. In many of these studies, axial deformation was neglected and the average axial force was assumed to be constant over the length of the beam element. However, subsequent analysis showed that axial displacements could not be neglected in any nonlinear studies [57].

1.4. Natural Frequencies and Mode Shapes

A change in the cantilever deflection or its natural frequency can be employed to measure various parameters of a fluid. Any amount of added mass present on the surface of the cantilever would change its deflection and natural frequency. In this section, a brief literature review is provided on free vibration analysis of cantilever structures.

Evensen [58] showed that, for higher modes of vibration, the amplitude-frequency curves of a clamped-clamped beam or a clamped-free beam tend to approach that of a simply supported beam. The influence of the boundary conditions on the response becomes less pronounced as the mode number increases. Lee et al. [59] considered only the first mode of vibration in their analysis, while the work of Basak et al. [60], as involving higher harmonics and different mode types, represented the most complete work about a full computational approach to the FSI problem. Mode properties and resonance frequencies in a viscous fluid were calculated by Ricci [61] through an eigen frequency analysis to avoid the time domain simulation. Da Lozzo et al. [62] developed a simple formula for calculating the added mass to be used in estimation of natural frequencies of uniform circular cantilever beam partially submerged in water where the finite element method was used to analyze the natural frequencies of the equivalent coupled fluid-structure system. Sader et al. [63] performed a theoretical analysis of the frequency response of the cantilever beam immersed in a viscous fluid and excited by an arbitrary force. The arbitrary force, in this case had been assumed to be thermal, i.e., Brownian motion of the molecules of the surrounding fluid. In this model, the undamped modes of cantilever were considered and the deflection of the cantilever was assumed to be a sum of these modes where each mode is excited by the Brownian motion of fluid particles. They presented numerical results

of deflection response of AFM cantilevers in their model. To calculate the eigen frequencies of a beam analytically, Van Eysden and Sader [64] published an enhanced model. Previously, Elmer and Dreier [65] noted already that the added mass on a submerged cantilever beam was frequency dependent, with the highest influence at low frequencies.

1.5. Computational Modeling

The interaction of a flexible structure submerged in a fluid gives rise to a variety of physical phenomena with applications in many fields of engineering, such as stability and response of aircraft wings, flow of blood through arteries, response of bridges and tall buildings to winds, vibration of turbine and compressor blades, and vibration of cantilevers in fluid. FSI takes place when fluid flow causes deformation of the structure and deformation of the structure changes boundary conditions of the fluid flow. The cantilever-based FSI systems include Atomic Scope Microscopes, flow sensors, density and viscosity sensors, and the frequency response of such systems is an important parameter in order to understand the behavior of such physical systems where both fluid and solid domains have to be modeled. There are many applications where cantilevers are made to vibrate under the action of fluid flow.

The fluid-structure interaction appears as a physical phenomenon in engineering [67] such as static load, drag, and flow-induced-vibrations (FIV). The oscillation of the flexible structure in the fluid environment represents the most typical FSI problem. Zhang et al. [68, 69] considered the long and slender cantilever (i.e. $l \gg w$, where l and w were represented the cantilever length and width, respectively) so that it was possible to simplify the analysis, restricting the attention to the vibration of the cantilever cross-section in a two dimensional fluid domain. Such an approach, despite of the advantage of being certainly less time-consuming than

a three- dimensional one, becomes less accurate with the increase of mode number or the reduction of the beam aspect ratio l/w since, in both cases, fluid flow ceased to possess a genuine 2D nature.

G. Rezazadeh et al. [70] performed numerical analysis on electrostatically actuated micro beam in an incompressible, inviscid and stationary fluid. He used Lucey and Carpenter's theory [71] to express pressure loading on the cantilever beam in order to find non-dimensional added mass. This added mass had been used into Euler-Bernoulli equation to find the frequency response of the beam under fluid loading. Wang et al. [72] considered flow-induced vibration of cylinders with large aspect ratios. In his model, the structural part was solved by Euler-Bernoulli theory using normal modes while fluid forces are calculated by finite element method. Houston et al. [73] determined vibration characteristics of atomic force microscope cantilever operating in liquid. In his work, the behavior of the cantilever was simulated simultaneously with the time dependent flow field. The flow field was solved at each time step from the new cantilever velocity.

A fully coupled simulation of three dimensional problems involving fluid-structure interactions is the most accurate way to predict the behavior of high aspect ratio cylinders in cross flows. Borges et al. [74] used the combination of the Cosserat theory applied to slender beams, and the Immersed Boundary Methodology, which represented the interactions between the structural and fluid domains. They described the dynamic behavior of cylindrical structures with various levels of bending flexibility subjected to transverse flows characterized by different values of the Reynolds number. In FSI, the structural deformation of the structural object considered by Cesur and Feymark [75] was highly dependent on the surface forces induced by

the flow. In order to validate the prediction of these forces a nondeforming oscillating cylinder in a steady flow was chosen as the first FSI benchmark case.

1.6. Multiple Hair Sensors

The advent of miniature sensing devices had been quite rapid since micro fabrication techniques were developed. Micro flow sensors, micro cantilevers, micro pumps, micro viscosity sensors, micro valves are some of the examples of the micro fluidic devices that involve the fluidic structure interaction. MEMS cantilevers are used as sensors, transducers, probes, needles, transport mechanisms, resonators, latches, switches and relays. Vashist [76] studied the micro cantilevers diverse applications in sensing mechanisms. The response of a micro cantilever was utilized to measure many parameters such as flow rate, fluid pressure, density, viscosity etc. The deflection of the beams caused change in the cross-sectional area further causing change in the resistance of the piezoresistor. The flow velocity and direction were calculated by measuring this change in the resistance. Krijnen et al. [77] showed the functional acoustic flow sensor arrays based on the mechano-hair sensors found on crickets.

Several research groups had been working on modeling, fabrication, and optimization of biomimetic flow-sensing devices consisting of arrays of many flow sensors including hair-to-hair interactions. MEMS fabrication technology is very practical in the realization of these devices for its capabilities of parallel fabrication and integration of flow sensors into large sensor arrays. The additional value of this type of arrays is that the flow-sensitive hairs allow measurement of flows with high spatial resolution and therefore could facilitate complex flow pattern measurements. Several types of biomimetic flow-sensors found in the literature incorporated

various transduction mechanisms. These included piezoresistive sensing [78], capacitive sensing [79] and switching [80].

Bruinink et al. [81] described the successful continuation of the fabrication and design of flow-sensor arrays with capacitive sensing for reasons of high intrinsic sensitivity in combination with low power dissipation and promising performance. Casas et al. [82] investigated the viscous coupling effects of arrayed cantilevers in the parallel flow system where the flow was in the direction defined by the plane of the two hairs. Lewin et al. [83] investigated hair-hair interaction between pairs of hairs and quantified the viscous coupling of computational fluid dynamics (CFD) model for one or more hairs with a rigid body dynamics model for simulating both biological and artificial MEMS-based systems. Fu and Price [84] studied vibration responses of cantilevered vertical and horizontal square plates partially and fully submerged in fluid. The effect of submerged plate length on the resonant frequencies of plates had been investigated in their work.

Chapter 2

Natural Frequency and Mode Shapes of the Hair Receptor

To understand the fluid-structure interaction problem, it is essential to study the vibrations of the flexible structures. Some of the examples of flexible structures are listed below.

Examples of flexible structures in the dynamic system applications are:

1. One-dimensional structures: Beams, Strings, and Shafts
2. Two-dimensional structures: Membranes and Plates
3. Three-dimensional structures: Shells

In the present study, biomimetic hair receptors are investigated in order to determine their fundamental frequencies and mode shapes similar to the cantilever beam applications to understand the fluid-structure interaction problems more efficiently.

In the absence of any fluid (i.e. in vacuum), without the action of any external force, analysis of natural frequencies of a hair receptor can be solved by the Euler-Bernoulli beam theory. Natural frequencies are required in order to study the response of microstructures when they are excited at its one of their frequencies. This phenomenon is also known as resonance.

2.1. Assumptions

In the present study, a set of assumptions are made for the hair receptor in structural domain as follows.

1. The hair structure has uniform cross-section and the deflection of the hair receptor is elastic and linear so that Hooke's law is valid.
2. The effect of shear deformation and rotary inertia of the hair receptor are small enough to be neglected as compared to the bending deflection
3. Plane sections of the hair receptor remains plane after deformation.
4. The plane of symmetry of the hair receptor is also the plane of vibration so that rotation and translation are decoupled

2.2. Euler-Bernoulli Equation of Motion of Hair Receptor

A beam is a simple structure which has one of its dimensions much larger than the other two. Beam theory is defined based on the following assumptions which are also known as Euler-Bernoulli assumptions [85].

1. Cross-sections of the beam do not deform in a significant manner under the application of transverse or axial loads and it can be assumed as rigid
2. During deformation, the cross-section of the beam is assumed to remain planar and normal to the deformed axis of the beam

In the Euler-Bernoulli Beam theory, effects of rotary inertia and shear deformation are neglected. When a cantilever beam like hair receptor oscillates freely in a vacuum, the characteristics equation or frequency equation gives the natural frequency. From the expression of the natural frequencies, they depend only on the geometric and material properties of the hair structure. It is to note that, the free vibration equation for the hair receptor is valid for vibration in a vacuum which means that, no damping is there or in a medium in which damping is almost zero. When the force is removed from a displaced hair receptor, the hair receptor will return to

its original shape. However, inertia of the hair receptor will cause the hair to vibrate around that initial location. Here the elastic modulus (E), inertia (I), and cross-sectional area (A_s) are assumed constant along the hair length [86].

In this study, cantilever beam application is utilized to understand the FSI analysis of the hair receptor which is attached to the flat plate more accurately and efficiently. One of the hair receptors end is fabricated to the flat plate at the base and the other end moves freely such that it supports the cantilever beam application as shown in Fig. 1. The cylindrical hair receptor is assumed to have uniform cross-section that undergoes small deflection for small slope where linear elastic region (Hooke's law) is validated.

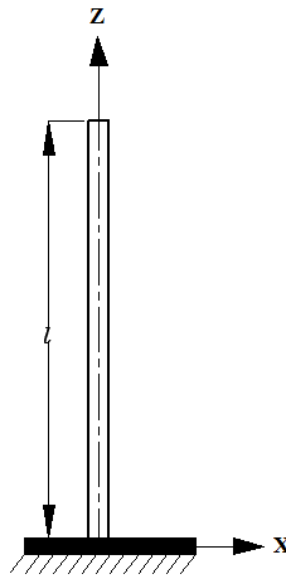


Figure 1: A clamped-free cylindrical (beam) hair receptor

Euler-Bernoulli equation of motion of beam for the hair receptor in the absence of an external force is expressed as [86]

$$EI \frac{\partial^4 w(z, t)}{\partial z^4} = -\rho A_s \frac{\partial^2 w(z, t)}{\partial t^2} \quad (1)$$

Let $\lambda = \sqrt{\frac{EI}{\rho A_s}}$, then equation (1) becomes,

$$\lambda^2 \frac{\partial^4 w(z, t)}{\partial z^4} = -\frac{\partial^2 w(z, t)}{\partial t^2} \quad (2)$$

The above equation is solved by separation of variables method [87]. Assume that the displacement is separated into two parts; one depends on position and another on time as shown in the following form.

$$w(z, t) = W(z)T(t) \quad (3)$$

where $W(z)$ is a function of shape and independent of time as well as $T(t)$ is a function of time and independent of position.

Substituting Equation (2) into Equation (1),

$$\lambda^2 \frac{\partial^4 (W(z)T(t))}{\partial z^4} = -\frac{\partial^2 (W(z)T(t))}{\partial t^2}$$

Dividing the above equation by $W(z)T(t)$,

$$\frac{\lambda^2}{W(z)} \frac{d^4 W(z)}{dz^4} = -\frac{1}{T(t)} \frac{d^2 T(t)}{dt^2} = \omega_n^2 \quad (4)$$

Since the left side of equation (4) does not change as t varies, the right side must be a constant. Similarly, since the right half of the equation (4) does not change as z varies, the left

half must be a constant. Because each side is constant, equation (3) is valid and the method of separation of variables can be used.

Let this constant be denoted as ω_n^2 . It can be shown that ω_n^2 is a real quantity, and that ω_n are natural frequencies of the hair receptor.

Equation (4) is written as

$$\frac{d^2W(z)}{dz^2} - \beta^4W(z) = 0 \quad (5)$$

where $\beta^4 = \frac{\rho A_s \omega_n^2}{EI}$

$W(z)$, is assumed to be in the form of,

$$W(z) = B_1e^{\beta z} + B_2e^{-\beta z} + B_3e^{i\beta z} + B_4e^{-i\beta z} \quad (6)$$

where $B_1, B_2, B_3,$ and B_4 are constants.

Equation (6) can also be expressed in a linear combination of trigonometric equations as follows

$$W(z) = C_1 \cos(\beta z) + C_2 \sin(\beta z) + C_3 \cos h(\beta z) + C_4 \sinh(\beta z) \quad (7)$$

where $C_1, C_2, C_3,$ and C_4 are constants.

2.3. Natural Frequencies of a Hair Receptor

When a system is given an initial input and then set to vibrate, it is said to be vibrating freely. In this case, the system is said to be vibrating at one or more of its natural frequencies. In the present model, hair receptor is considered as cantilever beam, free at one end and fixed at the other end. The fixed end must have zero displacement and zero slope due to clamped boundary condition. The free end cannot have a bending moment or shearing force.

The following boundary conditions are considered for the cantilever hair receptor,

1. At fixed end,

The deflection at the base is zero,

$$W = 0 \quad (8)$$

The slope at the wall is horizontal,

$$\frac{dW}{dz} = 0 \quad (9)$$

2. At free end,

The bending moment at the free end is zero,

$$\frac{d^2W(l)}{dz^2} = 0 \quad (10)$$

The shear force acting at the free end is zero

$$\frac{d^3W(l)}{dz^3} = 0 \quad (11)$$

Using the first boundary condition in equation (7), at the fixed end,

$$C_1 = -C_3 \quad (12)$$

Applying the second two boundary conditions at the fixed end in equation (7),

$$C_2 = -C_4 \quad (13)$$

By using the boundary conditions at the free end and solving to get,

$$C_1 \cos(\beta l) + C_2 \sin(\beta l) - C_3 \cos h(\beta l) - C_4 \sinh(\beta l) = 0 \quad (14)$$

$$C_1 \sin(\beta l) - C_2 \cos(\beta l) + C_3 \sin h(\beta l) + C_4 \cosh(\beta l) = 0 \quad (15)$$

These four boundary conditions produce four equations (12 through 15) with the four unknown coefficients C_1 , C_2 , C_3 , and C_4 . These can be written as the single vector equation.

$$\begin{bmatrix} 1 & 0 & 1 & 0 \\ 0 & 1 & 0 & 1 \\ \cos(\beta l) & \sin(\beta l) & -\cos h(\beta l) & -\sinh(\beta l) \\ \sin(\beta l) & -\cos(\beta l) & \sin h(\beta l) & \cosh(\beta l) \end{bmatrix} \begin{bmatrix} C_1 \\ C_2 \\ C_3 \\ C_4 \end{bmatrix} = \begin{bmatrix} 0 \\ 0 \\ 0 \\ 0 \end{bmatrix}$$

This vector equation can have a nonzero solution for the vector $\mathbf{C} = [C_1 \ C_2 \ C_3 \ C_4]^T$ only if the determinant of the coefficient matrix vanishes. Furthermore, since the coefficient matrix is singular, not all of the elements of the vector \mathbf{C} can be calculated.

Setting the determinant above equal to zero yields,

$$\cos \beta l \cosh \beta l = -1 \quad (16)$$

This is the characteristic frequency equation along with the roots for free vibration of a cantilever hair receptor in vacuum. This expression is satisfied for an infinite number of choices for β , denoted by β_n .

The solution can be visualized by plotting both $(\cos \beta l)$ and $(-1/\cosh \beta l)$ on the same plot. The first three solutions for the cantilever hair receptor are shown in the following Table 1.

Table 1: The first three eigenvalues of cantilever hair receptor model

n	$\beta_n l$
1	1.875
2	4.694
3	7.855

For the rest of the modes ($n > 5$), the solutions to the characteristic equation are well approximated by [86],

$$\beta_n l = \frac{(2n - 1)\pi}{2}$$

with these values of the weighted frequencies $\beta_n l$, the individual modes of vibration are calculated.

The natural frequencies of hair receptor at each mode are calculated by following expression.

$$\omega_n = (\beta_n)^2 \sqrt{\frac{EI}{\rho A_s}} \text{ rad/s} = (\beta_n l)^2 \times \frac{1}{2\pi} \sqrt{\frac{EI}{\rho A_s l^4}} \text{ Hz} \quad (17)$$

Using the above relationships, the first three natural frequencies are given as,

$$\text{First natural frequency, } \omega_1 = (1.875)^2 \times \frac{1}{2\pi} \sqrt{\frac{EI}{\rho A_s l^4}} \quad (18)$$

$$\text{Second natural frequency, } \omega_2 = (4.694)^2 \times \frac{1}{2\pi} \sqrt{\frac{EI}{\rho A_s l^4}} \quad (19)$$

$$\text{Third natural frequency, } \omega_3 = (7.855)^2 \times \frac{1}{2\pi} \sqrt{\frac{EI}{\rho A_s l^4}} \quad (20)$$

2.4. Mode Shapes of a Hair Receptor

Modal analysis is used to study dynamic behavior of the hair structure under vibrational frequency. There are a few numerical methods which can be found in the literature used to perform model analysis of structures modeled by the Euler-Bernoulli beam theory.

By substituting equations (12) and (13) into (15) yields

$$C_3 [\sinh(\beta l) - \sin(\beta l)] + C_4 [\cosh(\beta l) + \cos(\beta l)] = 0 \quad (21)$$

Thus,

$$C_4 = - \left(\frac{\sinh(\beta l) - \sin(\beta l)}{\cosh(\beta l) + \cos(\beta l)} \right) C_3$$

for each n . The fourth coefficient C_3 cannot be determined by this set of equations, because the coefficient matrix is singular. Otherwise, each C_i (where $i = 1, 2, 3$, and 4) would be zero. This remaining coefficient becomes the arbitrary magnitude of the eigenfunctions. As this constant depends on n , denote it by $(C_3)_n$. Substitution of these values of C_i in the expression of $W(z)$ for the spatial solution yields the result that the eigenfunctions or mode shapes of the form

$$W_n(z) = (C_3)_n \left[\cosh(\beta_n z) - \cos(\beta_n z) - \left(\frac{\sinh(\beta l) - \sin(\beta l)}{\cosh(\beta l) + \cos(\beta l)} \right) [\sinh(\beta_n z) - \sin(\beta_n z)] \right] \quad (22)$$

$n = 1, 2, 3 \dots$

The first three mode shapes are plotted in Fig. 2 for $(C_3)_n = 1$ and $n = 1, 2, 3$.

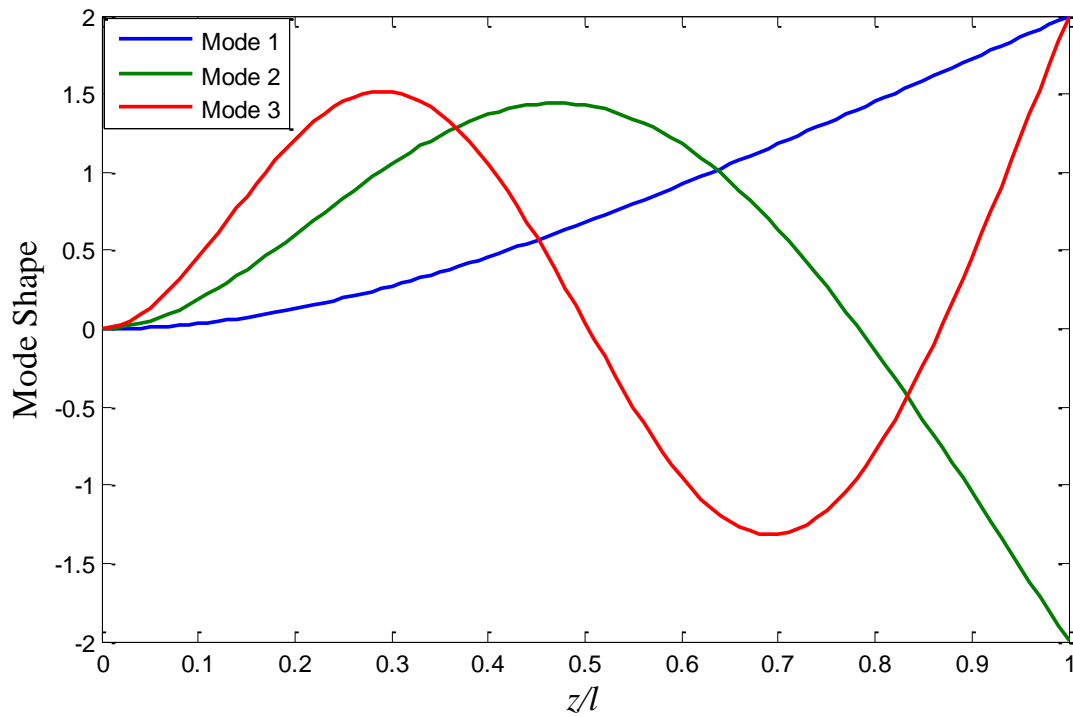


Figure 2: Plot of the first three mode shapes of the clamped-free hair structure

Chapter 3

Fluid-Structure Interaction

The fluid-structure interaction (FSI) phenomenon is the result of the interaction of multiple continuum fields. The fluid (gas or/and liquid) forces act on a neighboring elastic structure which is deformed and then it influences the flow of the adhering fluid. Due to the deformation of the structure, both the fluid velocity and the fluid domain change. The boundary conditions for the fluid and structural models represent the coupling mechanism between the fields. However, even though everything looks simple and clear; the accurate and efficient solution of FSI problems is still a highly complicated task and an open area of research. The computational fluid dynamics (CFD), computational structural dynamics (CSD), finite element method (FEM) provide us with specific mathematical models and numerical techniques that can be coupled to build a numerical solver for a FSI problem.

Several finite element simulation programs are available for the investigation of dynamic response of structures submerged in a fluid. Common programs suitable for the FSI are ABAQUS, ANSYS, and COMSOL. The commercially available finite element analysis package ABAQUS 6.12 [88] with CFD capabilities is used to develop the FSI model in this study. All the simulations are done in co-simulation engine, which is the FSI solver for Abaqus 6.12. The FSI model is a combination of both the CFD model for a fluid domain and the structural model for a solid domain. Furthermore, fluid flow is coupled with the FE model using the CFD.

3.1. CFD Model

The CFD models for the fluid domains of single hair receptor and multiple hair receptors studies are described below. In both studies, the rectangular enclosure is considered as the fluid domain which represents the surrounding air flowing over the hair receptor(s).

3.1.1. Single Hair Receptor Model

In a single hair receptor model, one hair receptor is considered as a cantilever structure immersed in the velocity driven fluid domain and attached to the flat plate.

In the CFD model, the fluid domain is chosen such that the inlet, outlet, and far field boundaries are far enough from the hair receptor's surface to avoid any boundary effects. In a single hair receptor model, the hair receptor is placed 2.0 mm away from the inlet boundary and 1.0 mm away from the side and top boundaries while the outlet boundary is placed 2.0 mm away from the center point of hair receptor. Thus, the fluid domain size is defined as $(4.0 \times 2.0 \times 2.0)$ mm³. The rectangular fluid domain with a single hair receptor [89] in the CFD model is shown in Fig. 3.

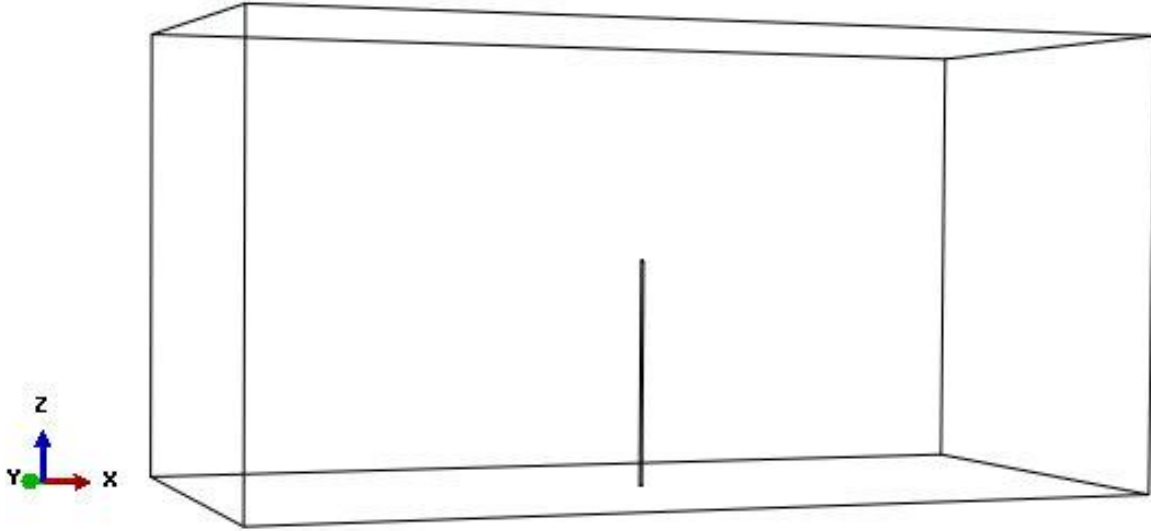


Figure 3: Computational domain for flow around a hair receptor

3.1.2. Multiple Hair Receptors Model

In the multiple hair receptors model, six hair receptors are considered as cantilever structures which are spaced in equal distances immersed in the velocity driven fluid domain and attached to the flat plate. This case is inspired from a multi cantilever study discussed by Paulo et al. [90].

In the CFD model, six hair receptors are placed in equal distance of 1.0 mm and the front row hair receptors placed 2.0 mm from the inlet boundary while the outlet boundary is placed 2.0 mm away from the rear hair ones. Finally, sides and top boundaries are placed 1.0 mm away, thus giving a fluid domain size of $(6.0 \times 3.0 \times 2.0) \text{ mm}^3$. The fluid domain is chosen such that the inlet, outlet, and far field boundaries are far enough from the hair receptor's surface to avoid any boundary effects. The rectangular fluid domain with multiple hair receptors in the CFD model is shown in Fig. 4.

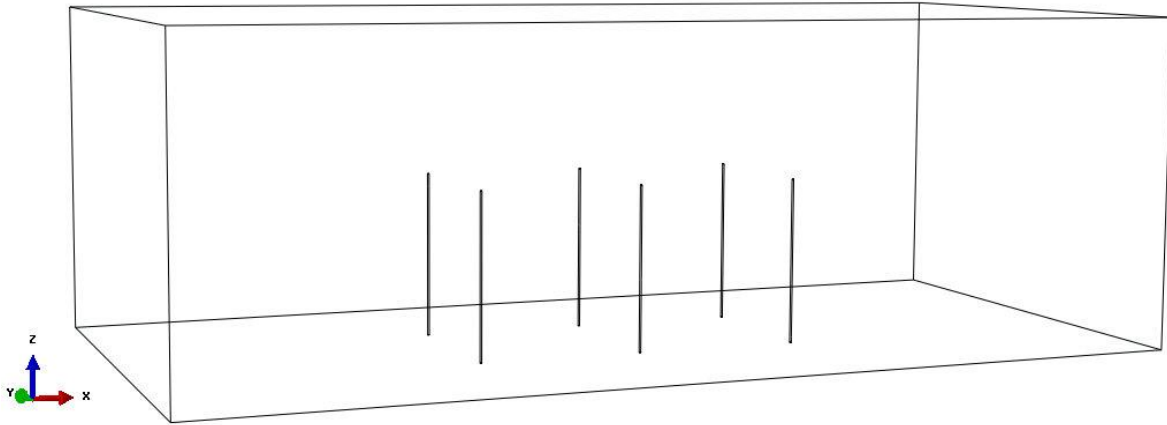


Figure 4: Computational domain for flow around multiple hair receptors

3.1.3. Fluid Properties

The fluid is modeled as an incompressible Newtonian fluid. Air properties at standard atmospheric conditions are assigned to the fluid in the CFD model as described in Table 2.

Table 2: Material properties for the CFD model

Air Properties	
Density, ρ , (Kg/m ³)	1.225
Dynamic Viscosity, μ , (Kg/m-sec)	1.78e-05

3.1.4. Mesh Generation

The fluid domain is meshed using C3D8R (eight-node linear brick, reduced integration, and hourglass control) and FC3D8 (eight-node linear fluid brick) types of elements. The computational meshing of the fluid domain with single hair receptor and multiple hair receptors are shown in Figs. 5 and 6, respectively. The mesh is refined near the hair receptors to

understand the flow behavior accurately and to resolve flow gradients near the surfaces. For this reason, it is meshed with a refined mesh with element size of 0.005 mm, whereas the rest of the domain is meshed with an approximate global element size of 0.2 mm by using the datum axis cell partition method to implement the mesh around the cylindrical hair receptor as shown in Fig. 7. However, the mesh used in this case presented here is adequate to show the boundary layer development over the flat plate surface. A total of 11,152 nodes with 9,175 elements are used to define the fluid domain in the single hair receptor model and 27,647 nodes with 24,210 elements are used in the multiple hair receptors model.

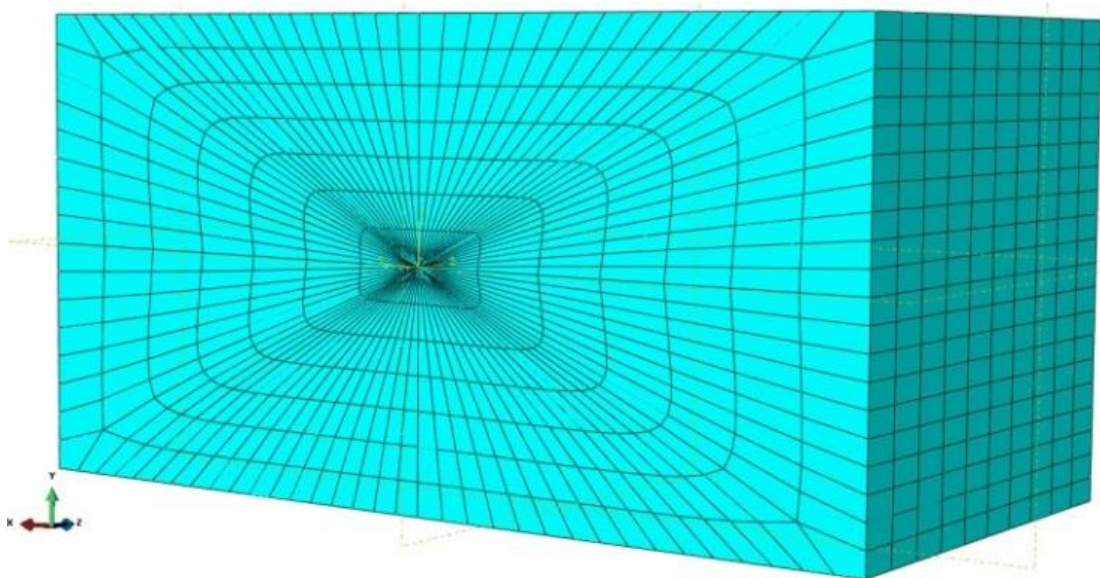


Figure 5: Computational meshing of the fluid domain with a single hair receptor

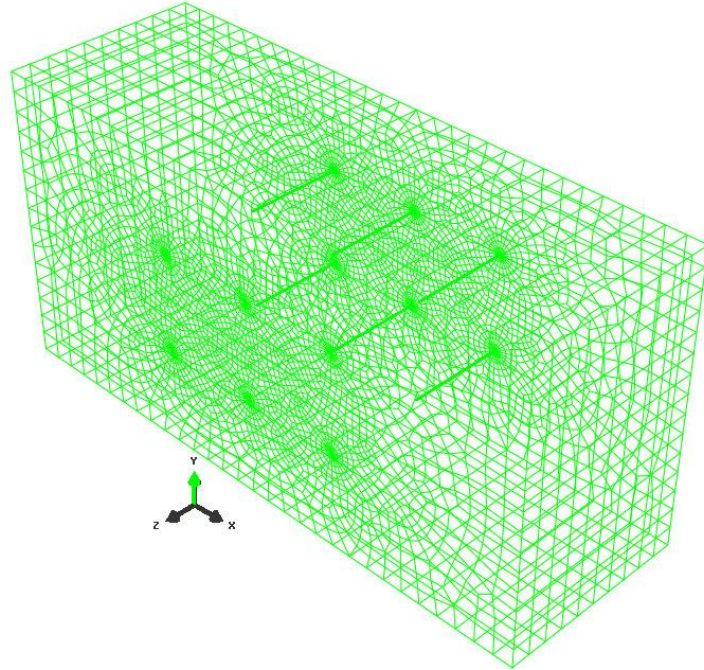


Figure 6: Computational meshing of the fluid domain with multiple hair receptors

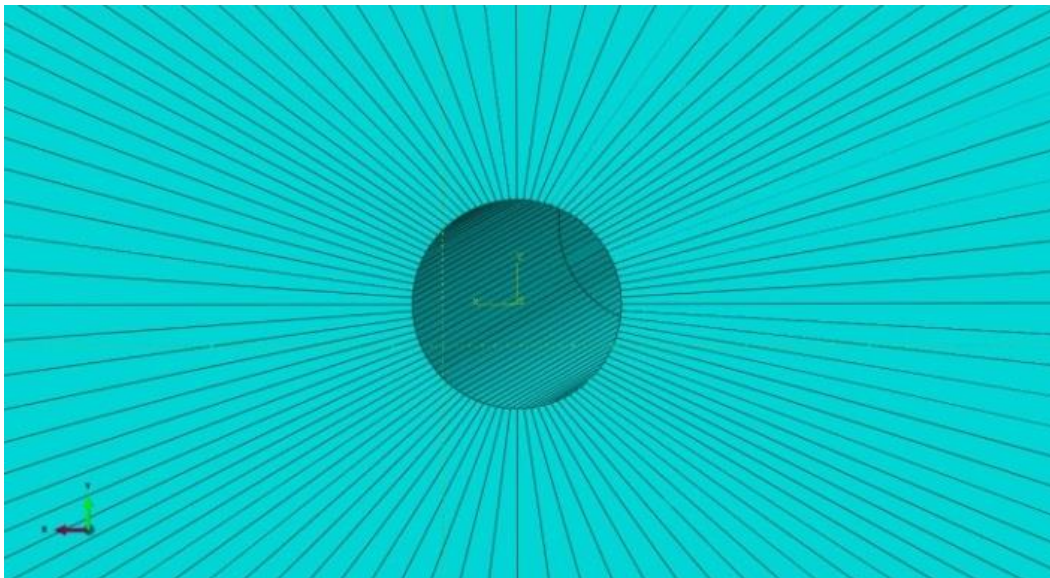


Figure 7: Meshing on the surface of the cylinder in fluid domain

3.1.5. Boundary Conditions on the Fluid

For both steady and unsteady flow across a flexible hair receptor, the following boundary conditions are applied to the fluid.

1. Inlet: For study flow, uniform incoming velocity ($V_x = \bar{V} = V_\infty$) of 0.1 m/s is assumed according to the average wind velocity sustained by hair receptors [35]. For unsteady flow, a periodic flow velocity of freestream is assumed. The following time-dependent velocity is prescribed using an amplitude definition:

$$V_x = \bar{V} + 0.1\bar{V}\sin(2\pi t)$$

2. Outlet: An outlet boundary condition is specified with the fluid pressure set to zero
3. Bottom Surface: A no-slip wall boundary condition is applied at the bottom surface of the fluid domain. All velocity components are set equal to zero. The bottom surface of the fluid domain is assumed as a flat plate on which hair receptors are mounted
4. Far-field: The far-field velocity is assumed to be equal to the inlet velocity. This is a reasonable choice if the far-field boundaries are far away from the hair receptor top surface. And, far-field boundaries are far enough such that the flow behavior doesn't affect the hair receptors
5. Symmetry: The velocity normal to the symmetry planes is assumed to be zero to constrain the out-of-plane flow

3.1.6. Boundary Conditions on the Mesh

Appropriate boundary conditions are also required for the mesh deformation solution.

1. Mesh Fixed: The mesh is fixed by prescribing zero-valued mesh displacement boundary conditions on the inlet, outlet, and the top surfaces
2. Mesh Symmetry: The mesh motion normal to the symmetry panes is constrained by prescribing $U_y = 0$ on sides of fluid domain

The following boundary conditions are specified mathematically on the fluid domain as shown in Table 3 for both steady and unsteady flow field.

Table 3: Boundary conditions for the CFD model

Boundary Condition	Steady Flows	Unsteady Flows
Inflow Velocity	$V_x = V_\infty, V_y = 0, V_z = 0$	$V_x = V_\infty = [\bar{V} + 0.1\bar{V}\sin(2\pi t)],$ $V_y = 0, V_z = 0$
Outflow Pressure	$P = 0$	$P = 0$
No-slip Condition	$V_x = 0, V_y = 0, V_z = 0$	$V_x = 0, V_y = 0, V_z = 0$
Symmetry Velocity	$V_y = 0$	$V_y = 0$
Far-field Velocity	$V_x = V_\infty, V_y = 0, V_z = 0$	$V_x = V_\infty = [\bar{V} + 0.1\bar{V}\sin(2\pi t)],$ $V_y = 0, V_z = 0$
Mesh Fixed	$U_x = 0, U_y = 0, U_z = 0$	$U_x = 0, U_y = 0, U_z = 0$
Mesh Symmetry	$U_y = 0$	$U_y = 0$

3.2. Structural Model

The structural model is described for a single hair receptor and multiple hair receptors as follows.

3.2.1. Single Hair Receptor Model

In the structural model, the hair receptor is modeled considering a 3-D flexible cylindrical cantilever beam. The thickness and length of the hair receptor is considered as 0.01 mm and 1.0 mm, respectively, thus giving l/d ratio equal to 100. The computational domain for a single hair receptor is shown in Fig. 8.

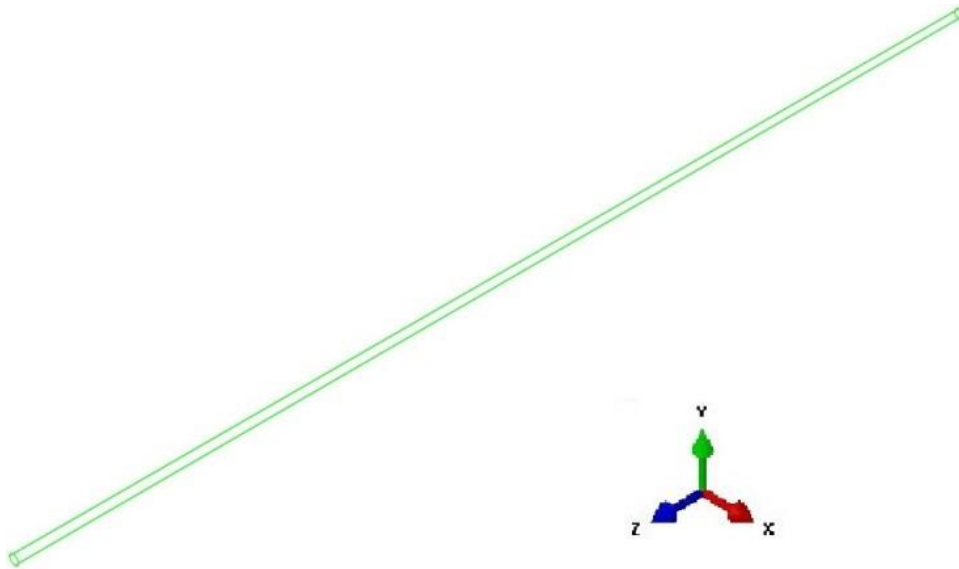


Figure 8: Computational domain of a single hair receptor

3.2.2. Multiple Hair Receptors Model

In the structural model, six hair receptors are modeled considering 3-D flexible cylindrical cantilever beams. The thickness and length of the hair receptors are considered as

0.01 mm and 1.0 mm, respectively, thus giving l/d ratio equal to 100. All the six hair receptors are placed at an equal distance of 1.0 mm from each another. The computational domain for the multiple hair receptors is shown in Fig. 9.

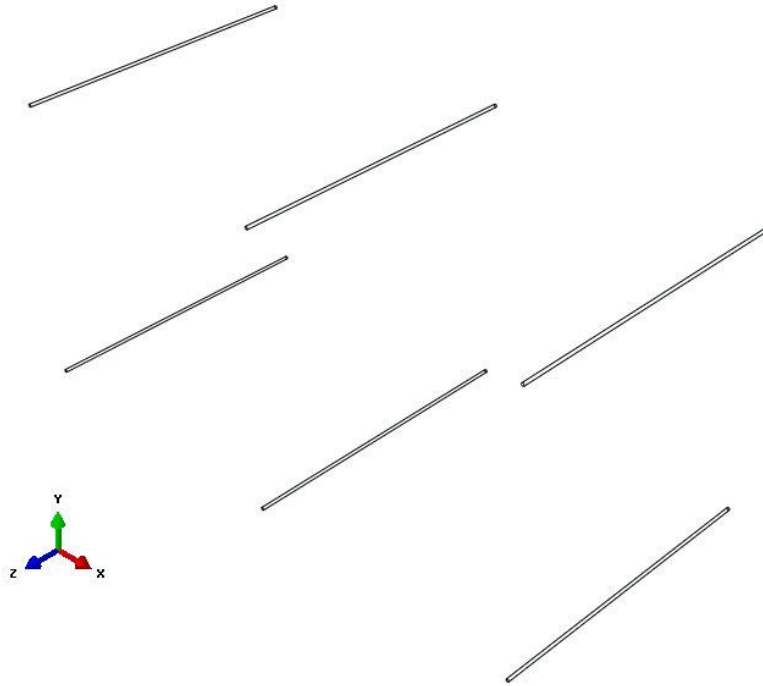


Figure 9: Computational domain of multiple hair receptors

3.2.3. Structural Properties

The material properties for the hair receptors are considered to be linearly elastic which allowed us to use the standard modulus of elasticity, density, and Poisson's ratio as shown in Table 4. Therefore, each hair structure is modeled as a viscoelastic cantilever beam with uniform diameter and material properties. While this may be consistent with artificial hairs, it is a geometric approximation to the tapered bat wing hair receptor as reported by Dickinson [35].

Table 4: Materials properties of the structural model

Polymer Properties	
Density, ρ_s , (kg/m ³)	1000
Young's modulus, E , Pa	10^7
Poisson ratio, ν	0.3

3.2.4. Mesh Generation

The solid domain is meshed using the first-order hexahedral stress/displacement elements (C3D8R eight-node linear brick, reduced integration, and hourglass control type of element) with the global element size of 0.005 mm as shown in Fig. 10. The computational mesh generated for multiple hair receptors is shown in Fig. 11. A total of 1,809 nodes with 800 elements are used to define the hair receptor in the single hair receptor model; and 5,454 nodes with 2,400 elements are used in the multiple hair receptors model.

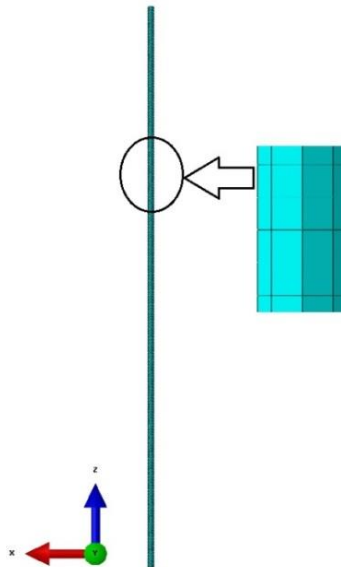


Figure 10: The mesh generated for the hair receptor

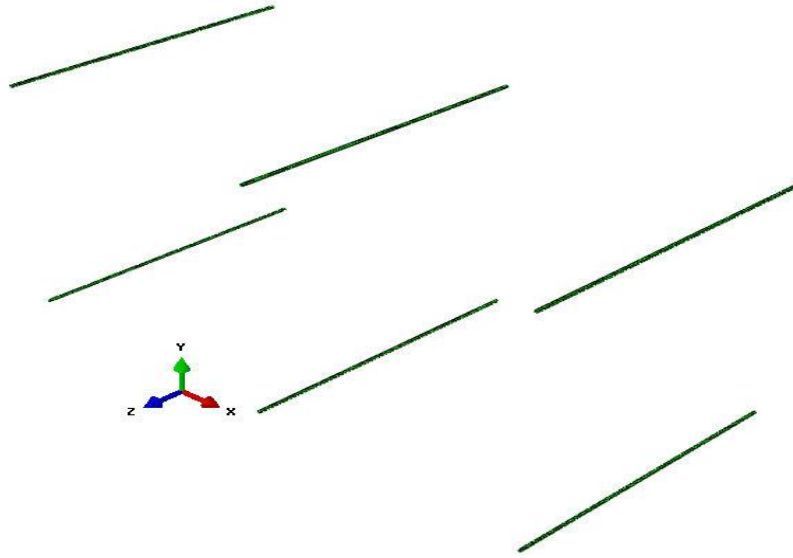


Figure 11: The mesh generated for multiple hair receptors

3.2.5. Boundary Conditions on the Hair Receptor

Since the hair receptor (s) is (are) mounted on the flat plate, the cantilever beam boundary conditions are applicable in this study. Therefore, the clamped boundary condition, where all the degrees of freedom are fixed, is specified at the root of the hair receptor whereas the other end is free to move in the flow field. The boundary conditions for the structural models are presented mathematically in Table 5.

Table 5: Boundary conditions for the structural model

Boundary Condition	Steady Flows	Unsteady Flows
Clamped Boundary	$U_x = 0, U_y = 0, U_z = 0,$ $UR_x = 0, UR_y = 0,$ $UR_z = 0$	$U_x = 0, U_y = 0, U_z = 0,$ $UR_x = 0, UR_y = 0,$ $UR_z = 0$

3.3. Fluid–Structure Interaction Analysis

The fluid-structure interaction (FSI) interface combines fluid flow with solid mechanics to capture the interaction between the fluid and the solid surface. Such behavior requires the structural and fluid equations to be solved independently and interface loads and boundary conditions to be exchanged after a converged increment. The FSI couplings appear on the boundaries between the fluid and the solid. The FSI interface uses an Arbitrary Lagrangian-Eulerian (ALE) method to combine the fluid flow formulated using an Eulerian description and a spatial frame with solid mechanics formulated using a Lagrangian description and a material (reference) frame.

In this study, the Abaqus/CFD model is coupled with the Abaqus/Standard structural model through the co-simulation engine. For the CFD model, the fluid-structure interface is assigned to the extruded cylindrical cavity inside the fluid domain. Similarly, the fluid-structure interface is defined on the surface of the hair receptor for the structural model. In single hair receptor model, fluid-structure co-simulation boundaries for both the CFD model and the structural model are presented in Figs. 12 and 13, respectively. For the FSI simulation, an incompressible laminar flow analysis step is selected in the CFD model while a dynamic-implicit step is selected in the structural model to determine the displacement of the hair receptor under steady and unsteady flow fields. An initial time increment of 0.0001s is used. However, the time increment can be changed depending on whether the structural or CFD model dictates the time increment size. The built-in time increment strategy is used where the co-simulation coupling time is chosen as the minimum of the time increments dictated by the structural and CFD models. The total simulation time is chosen to be 2.0 s.

In order to perform the FSI analysis, the Abaqus/Standard and Abaqus/CFD jobs need to be executed together. A co-simulation is performed where the two solvers exchange information at each co-simulation target time. The co-simulation target time is automatically chosen as the minimum of the time increments required by the structural and CFD solvers. In order to facilitate the co-simulation of the two analyses, the co-execution job procedure is used. A co-simulation job creates two analysis jobs and runs them simultaneously. It also automatically provides the driver options needed for communication between the two jobs.

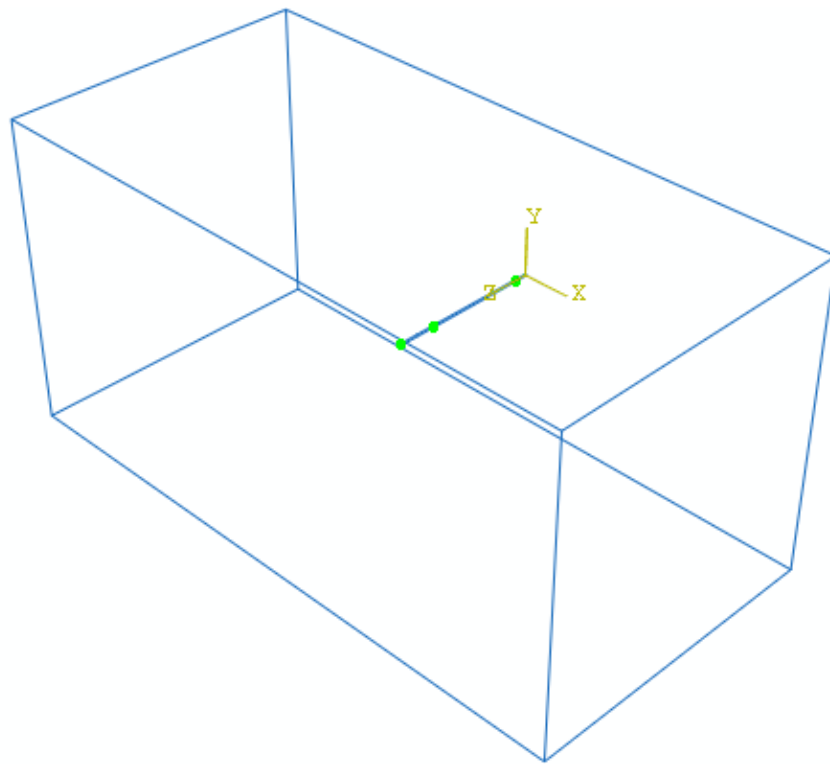


Figure 12: Illustration of fluid-structure co-simulation boundary in the fluid domain

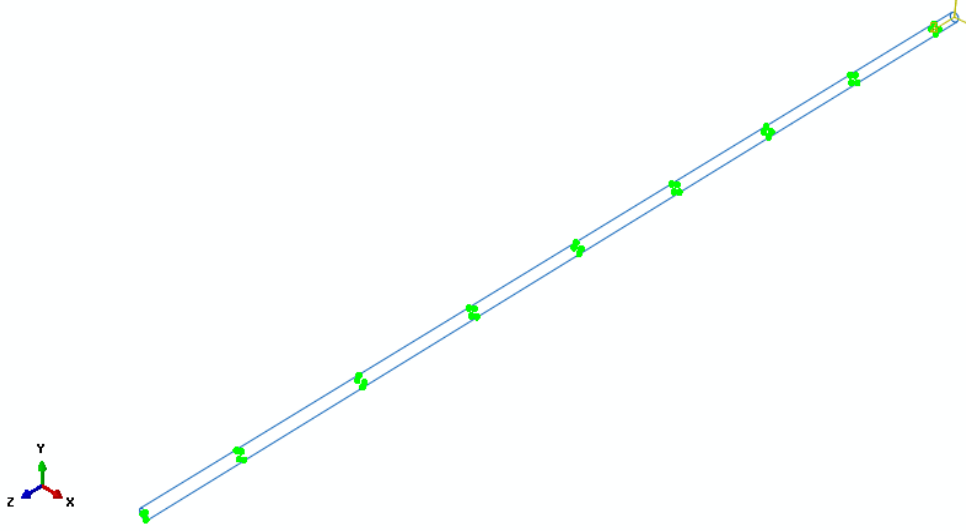


Figure 13: Illustration of fluid-structure co-simulation boundary in the structural domain

3.4. Solution Procedure

A fluid-structure interaction in its general form is described by the coupling of the equation of motion of the structure and the equation of motion of the fluid. The discretized equation of motion [92] of the structure is written as,

$$M_s \ddot{u} + D_s \dot{u} + K_s u = L_s \quad (23)$$

where M_s is the structural mass matrix, D_s is the structural damping matrix, K_s is the structural stiffness matrix, L_s the applied load vector, and u the nodal displacement vector where the dot denotes the time derivative.

The prediction of the velocity field as well as the pressure distributions in the fluid model requires the solution of the Navier-Stokes equations. The common equations for the fluid are the Navier-Stokes equations which are written in the general form [93] as:

$$\rho \left(\frac{\partial \vec{V}}{\partial t} + \vec{V} \cdot \nabla \vec{V} \right) = -\nabla P + \nabla \cdot \vec{\tau} + \vec{f} \quad (24)$$

where \vec{V} is the flow velocity vector, t is the time, ρ is the fluid density, P is the pressure, $\vec{\tau}$ is the deviatoric stress tensor, and \vec{f} represents body forces per unit volume acting on the fluid. For the full description of the fluid flow, additional information are needed like the equation for the conservation of mass, which is written as,

$$\frac{\partial \rho}{\partial t} + \nabla \cdot (\rho \vec{V}) = 0 \quad (25)$$

For the Navier-Stokes equations in its general form, no solution exists. Assumptions have to be made. Thus, the following assumptions are made for the present study.

1. The physical problem is approximated by using a three-dimensional model in Cartesian coordinates
2. The working fluid behaves like a Newtonian fluid with stokes assumptions
3. The flow is laminar and viscous
4. The fluid in contact with the wall is stationary (no-slip condition)
5. The physical properties of the fluid are assumed to be constant

Then the Navier-Stokes equations in their general form is reduced to

$$\rho \left(\frac{\partial \vec{V}}{\partial t} + \vec{V} \cdot \nabla \vec{V} \right) = -\nabla P + \mu \nabla^2 \vec{V} + \vec{f} \quad (26)$$

where the left side of equation (26) is the inertia force (per volume) which can be divided into the unsteady acceleration term $\frac{\partial \vec{V}}{\partial t}$ and the convective acceleration term $\vec{V} \cdot \nabla \vec{V}$. The right side of the equation is the divergence of the stress plus other body forces \vec{f} . The divergence of the stress is the sum of the pressure gradient $-\nabla P$ and the viscosity $\mu \nabla^2 \vec{V}$ with μ as the dynamic viscosity.

Also the equation for the conservation of mass is reduced to

$$\nabla \cdot \vec{V} = 0 \quad (27)$$

Boundary Conditions

The closure of any mathematical problem requires well-defined boundary conditions therefore the physical meaning of every condition at all different boundaries of the problem is considered very carefully and then expressed in an equivalent mathematical formula. At the inflow surface the fluid velocity is specified in component form as $(V_x, V_y, V_z) = (V_\infty, 0, 0)$. At the top surface far-field velocity condition is specified as $(V_x, V_y, V_z) = (V_\infty, 0, 0)$. At the outflow surface an outflow boundary condition is specified by setting the pressure $p = 0$ (the gradients of velocities are automatically set to zero for this boundary). On the bottom surface a no-slip boundary condition is enforced, given by $(V_x, V_y, V_z) = (0, 0, 0)$. Finally, the symmetrical boundary condition is applied on the lateral surfaces by prescribing $V_y = 0$.

Initial Conditions

The velocity, V , is set to zero everywhere in the flow domain. Velocity initial conditions that satisfy the solvability conditions for the incompressible Navier-Stokes equations are obtained by inserting the boundary conditions on the prescribed initial velocity field, followed by a projection to a divergence-free subspace. This mass adjustment to the velocity initial conditions is necessary to guarantee that the flow problem is well posed.

Chapter 4

Validation of Results

The results obtained from the FSI model should be validated with the benchmark results. The validation studies for structural model, fluid model, and FSI model are discussed in this chapter.

4.1. Validation of Structural Model

To validate the FE model, natural frequencies from the FE model are compared with those from the analytical solution of free vibration of cylindrical hair of length 1.0 mm and diameter 0.01 mm with clamped-free boundary condition [93].

Table 6: Comparison of natural frequencies of the hair receptor in a vacuum between FE model and analytical model

Natural Frequency, Hz	Analytical Model	FE Model (Case-I)		FE Model (Case-II)	
		Mesh Size =0.001, mm	% Diff.	Mesh Size =0.0005, mm	% Diff.
First Mode	139.83	138.79	0.741	139.66	0.119
Second Mode	876.34	869.51	0.779	874.94	0.160
Third Mode	2454.00	2433.40	0.839	2448.50	0.224

When the mesh size of the computational domain is 0.001 mm, the first three natural frequencies of the hair receptor in a vacuum are 138.79 Hz, 869.51 Hz, and 2,433.0 Hz, respectively, computed at 423,423 degrees of freedom. But the first three natural frequencies from the analytical solution are found to be 139.83 Hz, 876.34 Hz, and 2,454.0 Hz, respectively.

The natural frequencies of the hair in a vacuum between FE model and analytical model are compared quantitatively and shown in Table 6. When the mesh size of the computational domain is 0.0005 mm, the first three natural frequencies of the hair are 139.66 Hz, 874.94 Hz, and 2,448.5 Hz, respectively, computed at 3,007,503 degrees of freedom. The variation of the first three natural frequencies of the hair receptor is shown in Fig. 14.

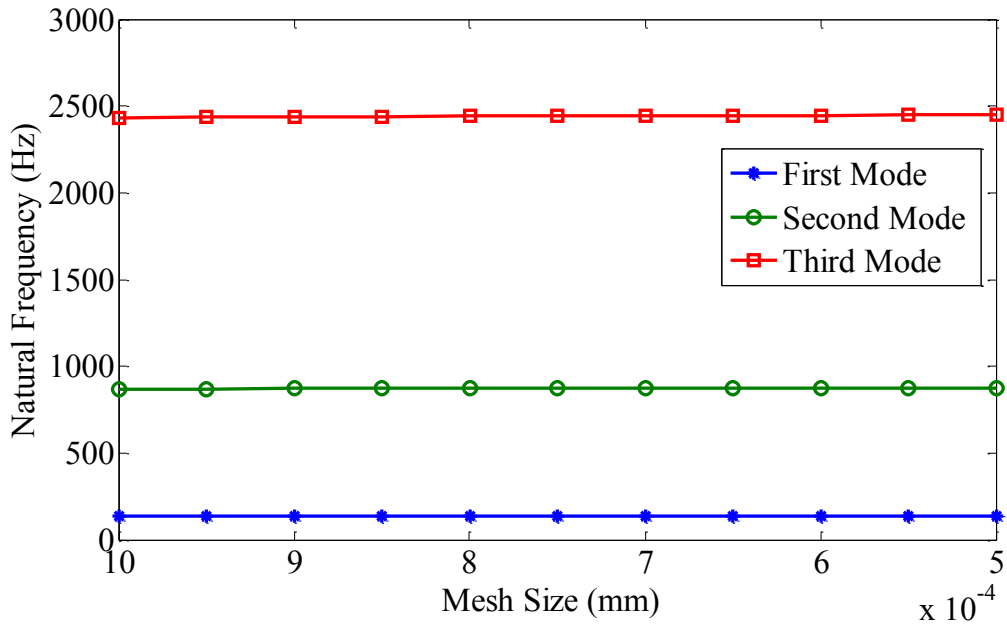


Figure 14: The variations of the first three natural frequencies of the hair receptor in a vacuum

The convergence of the natural frequencies of the cylindrical hair with clamped-free boundary conditions in a vacuum is studied and it is found that the frequencies converge between mesh size 0.001 mm and 0.0005 mm on the order of 1,000,000 degrees of freedom. It is noticed that the variations in the frequencies are very small (less than 1.0 %) with mesh size, which indicates that the model is converged at the finer mesh.

4.1.1. Mode Shapes of Hair Receptors

First three mode shapes of the hair in a vacuum are shown in Fig. 15. Mode shapes of the hair vary with the natural frequency. For higher frequencies, the mode shapes become more complex in shape. The total hair receptor motion is complex; each characteristic mode vibrates with a different shape and frequency. Mode shapes of the hair shows the location of the maximum deflection at the tip of the hair receptor.

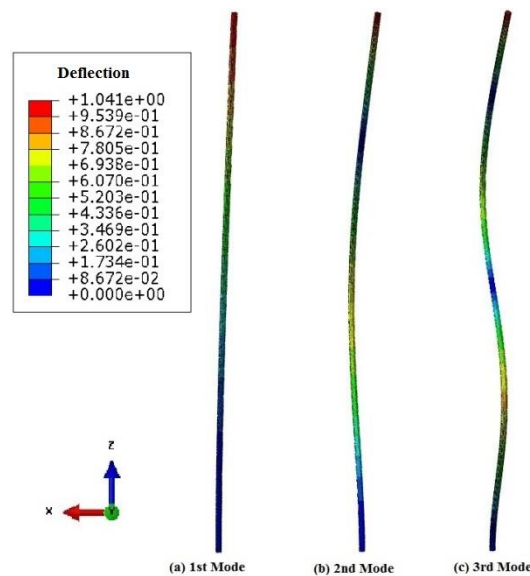


Figure 15: First, second, and third mode shapes of the hair receptor in a vacuum

4.2. Mesh Independence Study for FSI Simulation

To validate the FSI model, the mesh independence of the CFD model needs to be checked. For this, the hair receptor is simulated in the flow then refines the flow mesh without the hair to confirm mesh independence of the FSI solution. A case with steady airflow conditions and a freestream velocity of 100 mm/s is considered to perform different simulations in which the number of nodes of fluid model is varied while the ones from the structural models are kept

fixed. The mesh independence solution of the FSI solution is confirmed by selecting a point at the tip of hair receptor inside the fluid domain to show that the velocity magnitudes at this point converge as the grid is refined.

The variation of the velocity magnitude at a specific node with respect to the mesh of the CFD model is investigated and presented in Fig. 16. Fig. 16 indicates that the results from the FSI simulation are mesh independent for mesh grids in the CFD model with approximately 10,000 nodes or more.

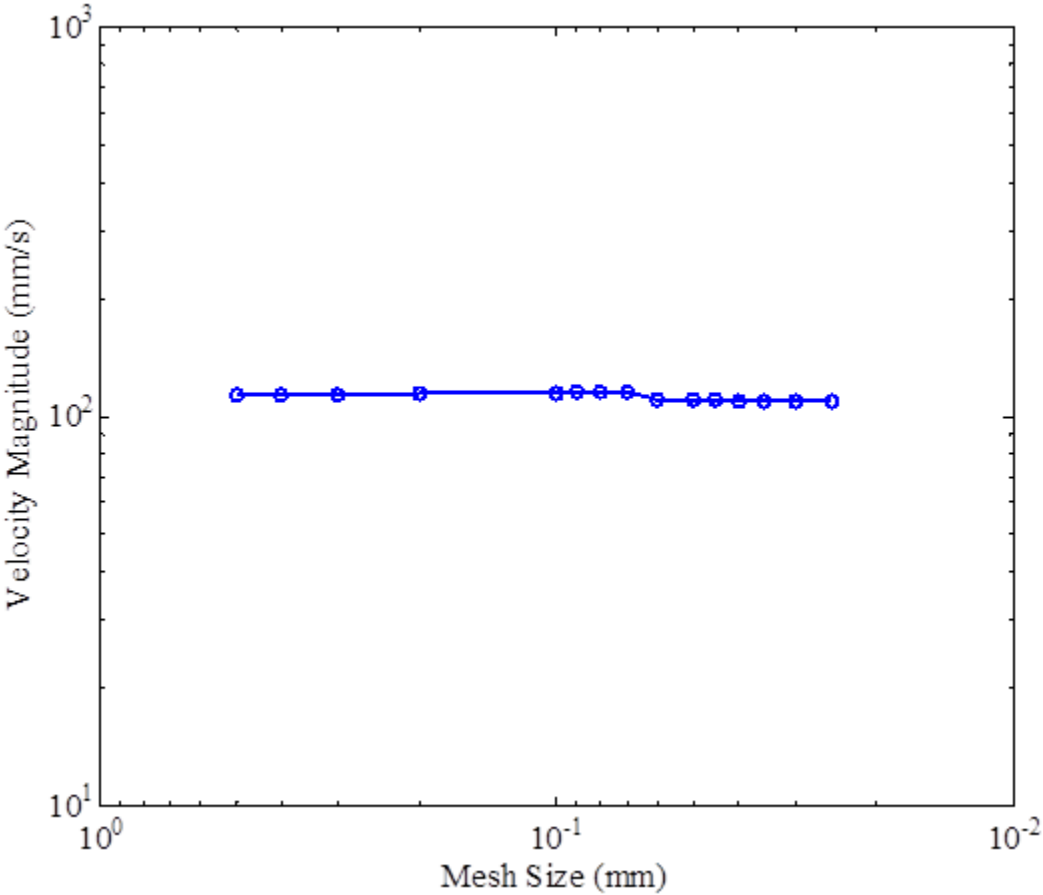


Figure 16: Mesh independence study for CFD model by monitoring the velocities at the tip of the hair receptor inside the fluid domain

4.3. Experimental Validation

The experimental validation of pressure on the cylindrical surface in terms of pressure coefficient C_p is also conducted in this study to understand the flow behavior surrounding the cantilever cylinder attached to the flat plate. To do this, pressure coefficient is compared over the upper or lower part of the cylinder because it is symmetrical with respect to x -axis. Also because of symmetry, the C_p values on the upper half of the cylinder are equal in magnitudes to the C_p values on the lower half of the cylinder. Therefore, the C_p values are compared with only upper half of the cylinder with experimental values at a mid-section of the cylinder length.

For this validation, a 2-D finite cylinder with the diameter of 0.03 m is studied that was used in the experiments by Park and Lee [94]. The freestream uniform inlet velocity is considered as 10.0 m/s which give Reynolds number of approximately 2×10^4 . The model consists of a 2-D cylinder in a rectangular domain as shown in Fig. 17. The inflow boundary is located 0.24 m upstream of the cylinder axis, the outflow boundary surface is located 0.72 m downstream of the cylinder axis, and the top and bottom surfaces are located 0.24 m away from the cylinder axis. The thickness of the cylinder is 0.005 m in the spanwise direction. The flow is modeled as three-dimensional but with the one element through the thickness and symmetry boundary conditions on the front and back faces to enforce 2-D conditions.

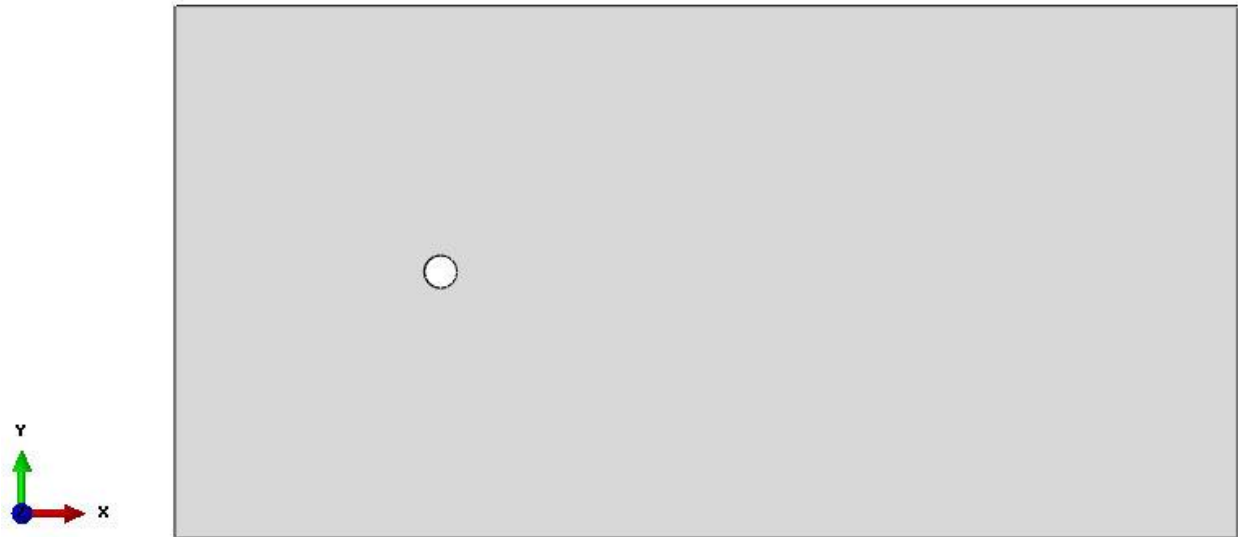


Figure 17: Model geometry for flow around the cylinder

This problem is characterized by boundary layer separation resulting from the adverse pressure gradients induced by the cylinder geometry. Over the forward portion of the cylinder, the surface pressure decreases from the stagnation point toward the shoulder. In this region, the boundary layer develops under a favorable pressure gradient where the net pressure force on a fluid element in the direction of the flow is sufficient to overcome the resisting shear force. Thus, motion of the element in the flow direction is maintained. However, the surface pressure eventually reaches a minimum and then begins increasing toward the rear of the cylinder. Thus, the boundary layer in this downstream region experiences an adverse pressure gradient. Since the pressure increases in the flow direction, a fluid element in the boundary layer experiences a net pressure force opposite to its direction of motion. At some point, the momentum of the fluid element will be sufficient to carry it into regions of increasing pressure. Here, the fluid adjacent to the solid surface is brought to rest, and flow separation from the surface occurs. As a result, wake is formed behind the cylinder in the low pressure region due to deficient in moment.

The C_p is obtained by dividing the difference between surface pressure (P) and a freestream pressure (P_∞) by the dynamic pressure [92], i.e.,

$$C_p = \frac{2(P - P_\infty)}{\rho V_\infty^2} = 1 - 4\sin^2\theta \quad (28)$$

However the pressure is variable along the vertical stagnation line. Therefore, data has been rescaled with a variable pressure $P_\infty(z)$ such that $C_p = 1.0$ for each altitude. The pressure distribution from the CFD simulation results are in a close agreement with the experimental values of Park and Lee [94] as shown in Fig. 18. The theoretical inviscid pressure distribution on a circular cylinder is also shown in Fig. 18. It is observed that the peak values almost overlap each other. The local minimum pressure is also predicted decently by all simulations, but the discrepancy is in the wake of the cylinder near 180 degrees where one can see a gradual increase in mean pressure values. This is due to the effect of separated flow and the subsequent failure of boundary layer theory. Since the Reynolds number is in the transition region, it develops smaller wake and higher pressure on the rear of cylinder.

The contour and vector plots of the velocity magnitudes as predicted from the CFD simulation are shown in Figs. 19 and 20. In Fig 20, the stagnation region at the front of the cylinder, and the wide wake region behind the cylinder can be clearly observed with defined regions of recirculation. Fig. 21 depicts that the pressure begins to have negative values at angles of $30 - 40^\circ$ approximately, as measured from the front of the cylinder.

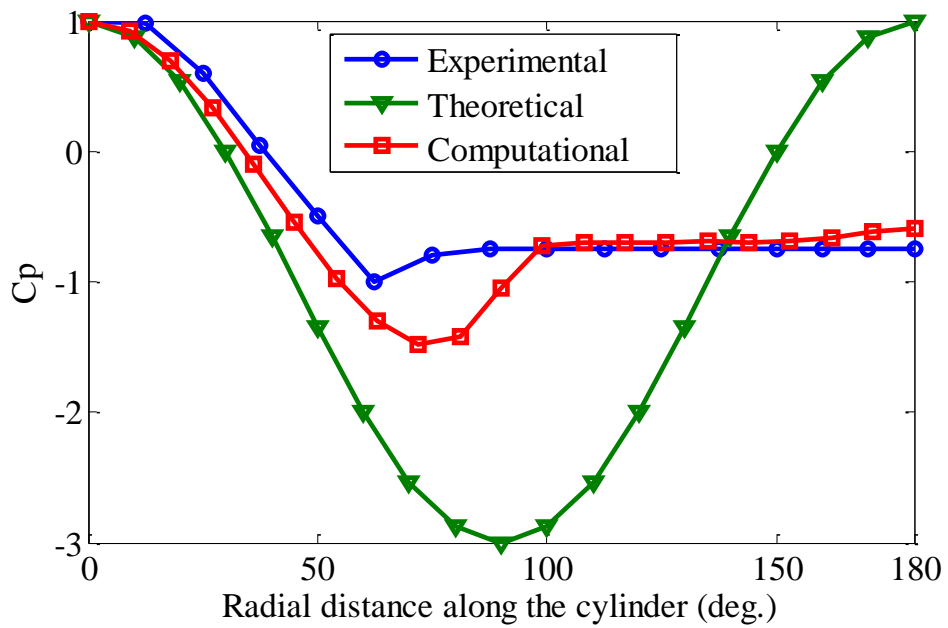


Figure 18: C_p distributions around the upper part of the cylinder surface

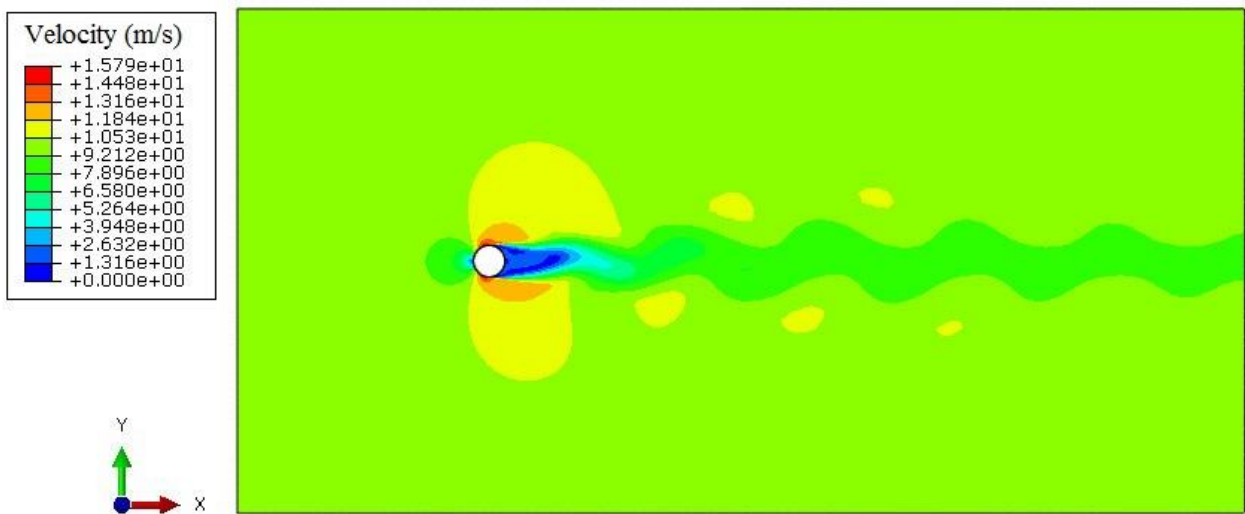


Figure 19: Velocity contours for flow around the cylinder

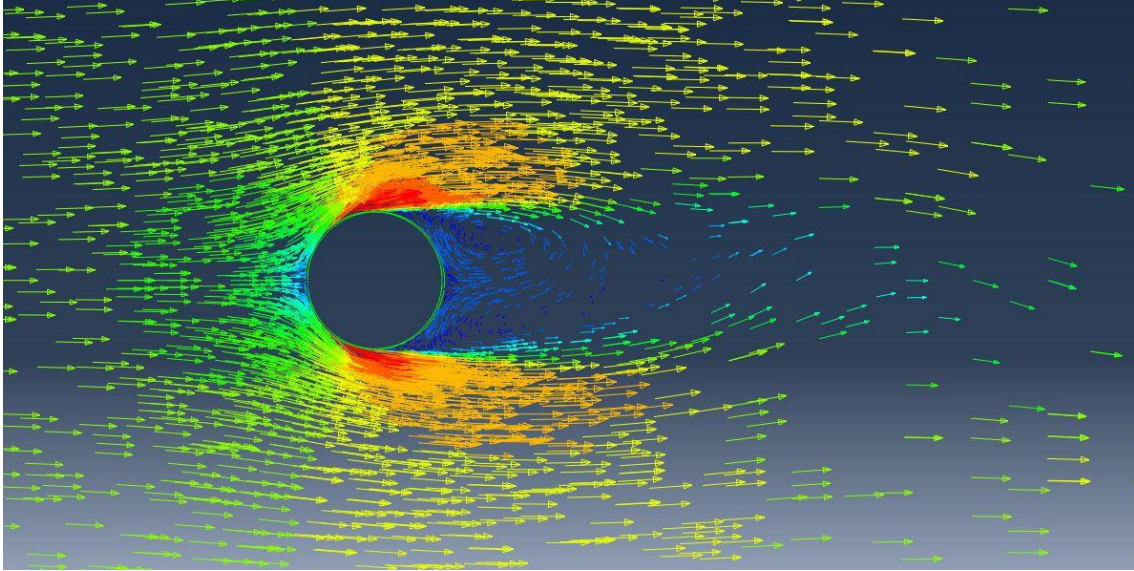


Figure 20: Velocity vectors for flow around the cylinder

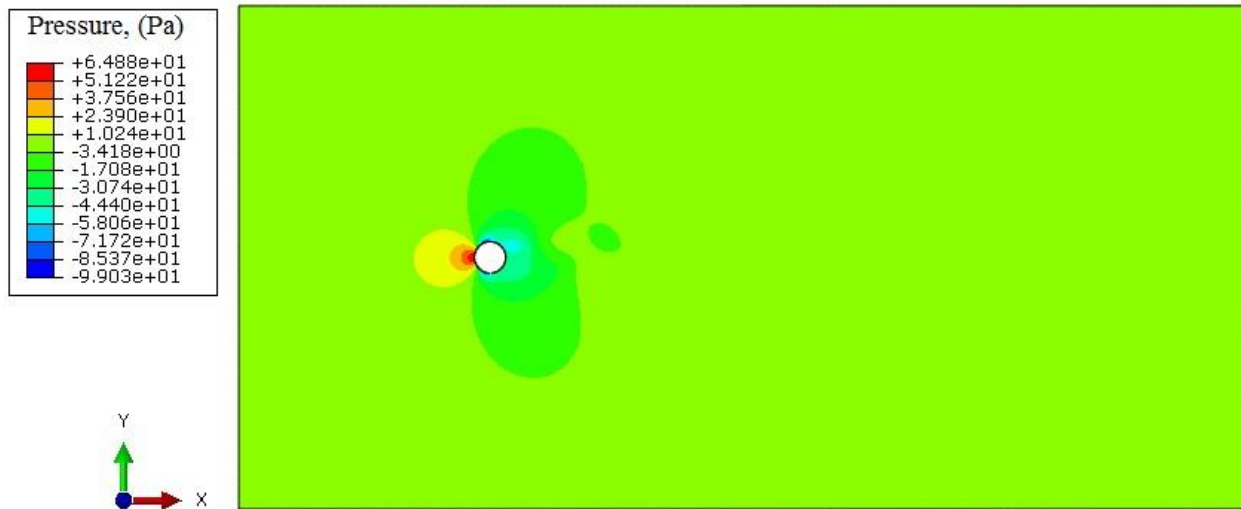


Figure 21: Pressure contours for flow around the cylinder

Chapter 5

Results and Discussion

The goal of modeling the hair receptor is to develop a relationship between nearby flow that applies surface forces to the hair. Hair receptor deforms due to the distributed load caused by the drag pressure of the moving air. This deformation, in turn, affects the flow field. To understand the dynamic properties of the hair influenced by the flow behavior, FSI analyses have been studied separately for single hair receptor and multiple hair receptors.

5.1. Single Hair Receptor Study

The single hair receptor model is evaluated for an exposed hair length of $l = 1\text{e-}3$ m, freestream velocity of $V_\infty = 0.1$ m/s and a characteristic diameter of the bat-scaled hair receptor $d = 1\text{e-}5$ m. To maintain a consistent boundary layer thickness evolution, the hair is assumed to reside 2.0 mm from the leading edge of a flat plate.

The results given by the co-execution of FSI model are considered at vertical mid-plane ($x = 0.0$ mm, $y = 1.0$ mm, $z = 0.0$ mm) to investigate the response of the hair receptor in both steady [0.1 m/s] and unsteady [$0.1 + 0.01 \sin(2\pi t)$ m/s] flow fields. The dynamic implicit method is used to perform the structural analysis of the hair receptor. In the unsteady flow, the periodic nature of the sinusoidal amplitude assigned to the inlet velocity is reflected on the velocity and deflection magnitudes. In contrast to the steady air flow, the velocity and deflection magnitudes are uniform in the flow field. The deflections and velocity magnitudes of the hair receptor at the tip for the time of 2.0 s in both steady and unsteady fluid flow field are shown in Figs. 22 and 23,

respectively. Initially, slight accelerated flow and higher deflections through fluid domain appear due to the effects of high viscous force and boundary layer development.

The deflection of the hair receptor at the tip is equal (2.544 times to the hair diameter) at the time of 0.5 s and 1.0 s for both steady and unsteady flow velocities. For unsteady flow, the hair receptor exhibits the maximum tip deflection (2.750 times to the hair diameter) at the time of 0.25 s and the minimum tip deflection (2.303 times to the hair diameter) at the time of 0.75 s. The flow velocities change similarly with time for both steady and unsteady flows. The presence of the fluid viscosity slows down the fluid particles very close to the solid surface and forms a thin slow moving fluid layer. The flow velocity is zero at the bottom surface of the computational domain and at the surface of the hair receptor to justify the no-slip boundary condition.

The deflection contour plots at four different times, i.e., 0.25 s, 0.5 s, 0.75 s, and 1.0 s are shown in Figs. 24 to 27 for steady flow and in Figs. 28 to 31 for unsteady flow to represent time-dependent results. The flow patterns over a cylindrical hair receptor at the time of 1.0 s are shown in Fig. 32 for steady flow and in Fig. 33 for unsteady flow. The pressure distributions around the hair receptor at the time of 1.0 s are shown in Fig. 34 for steady flow and in Fig. 35 for unsteady flow. The pressure starts to increase in the front side of the cylinder and decrease in the rear side of the cylinder.

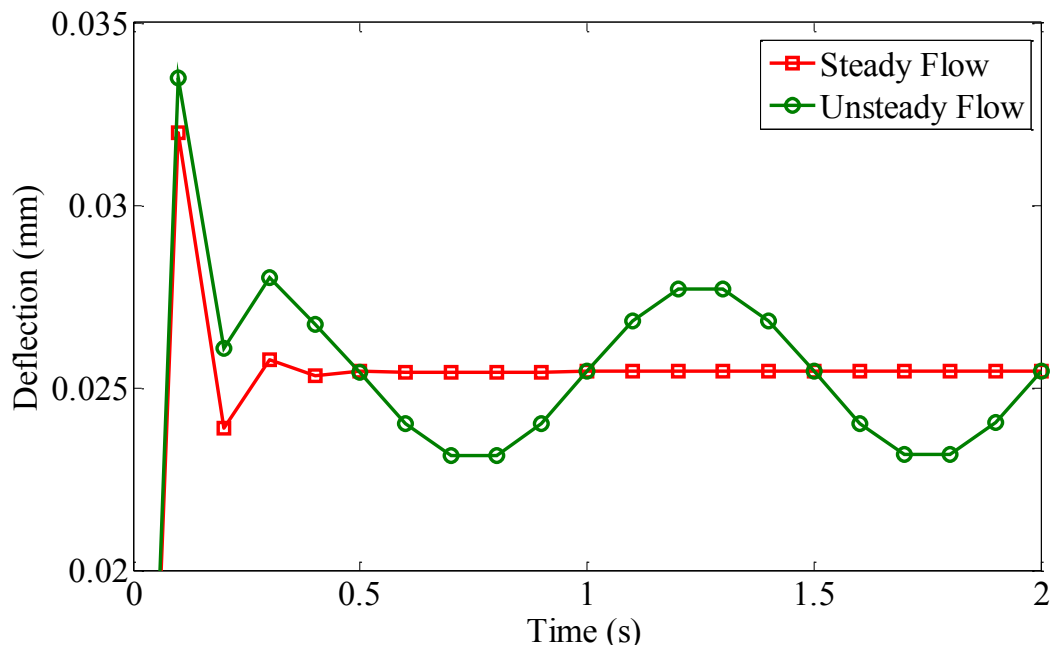


Figure 22: Time-varying deflections of the flexible hair receptor at the tip

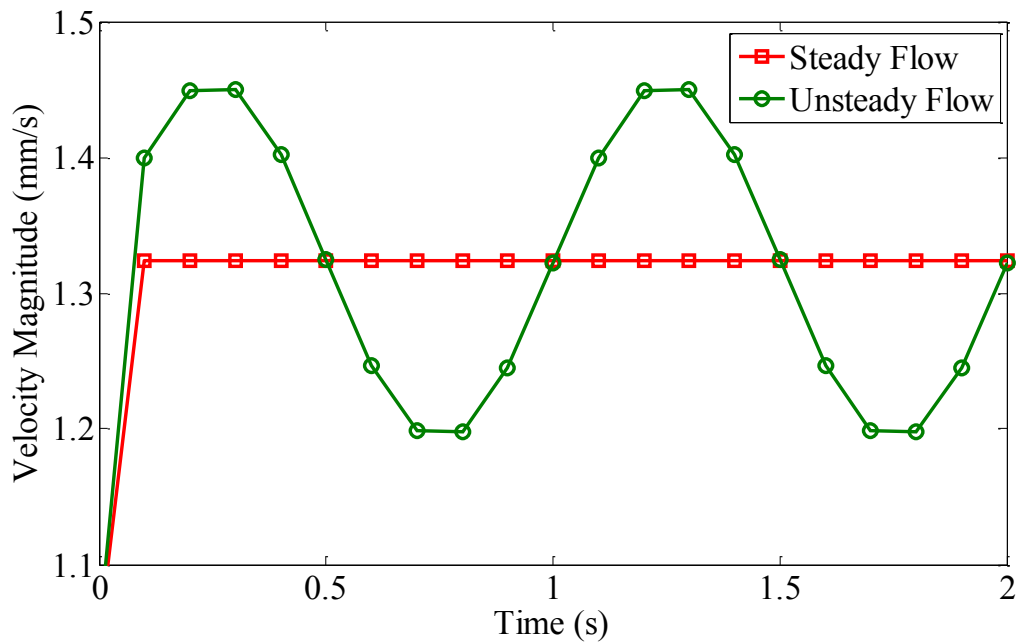


Figure 23: Time-varying velocity magnitudes of the flexible hair receptor at the tip

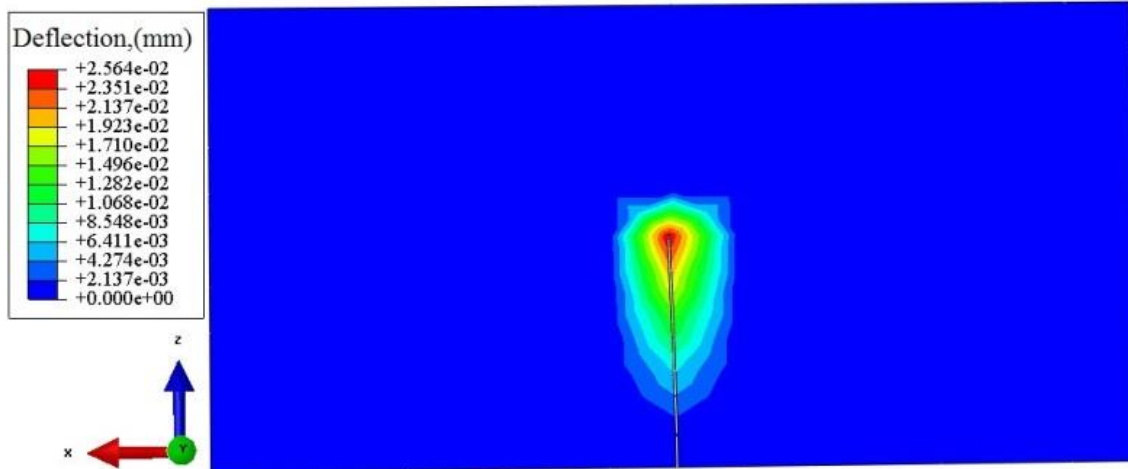


Figure 24: Deflection contour plot of the flexible hair receptor at the time of 0.25 seconds in steady flow

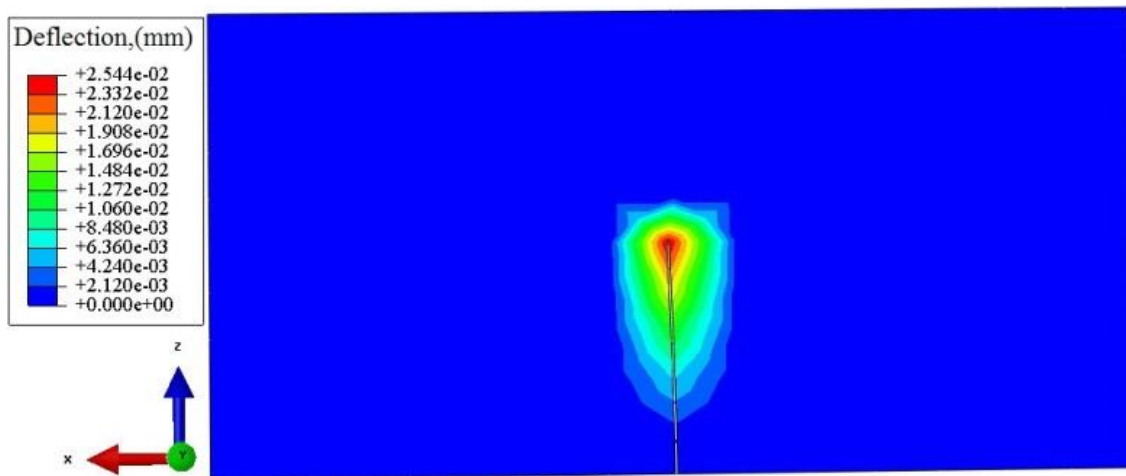


Figure 25: Deflection contour plot of the flexible hair receptor at the time of 0.50 seconds in steady flow

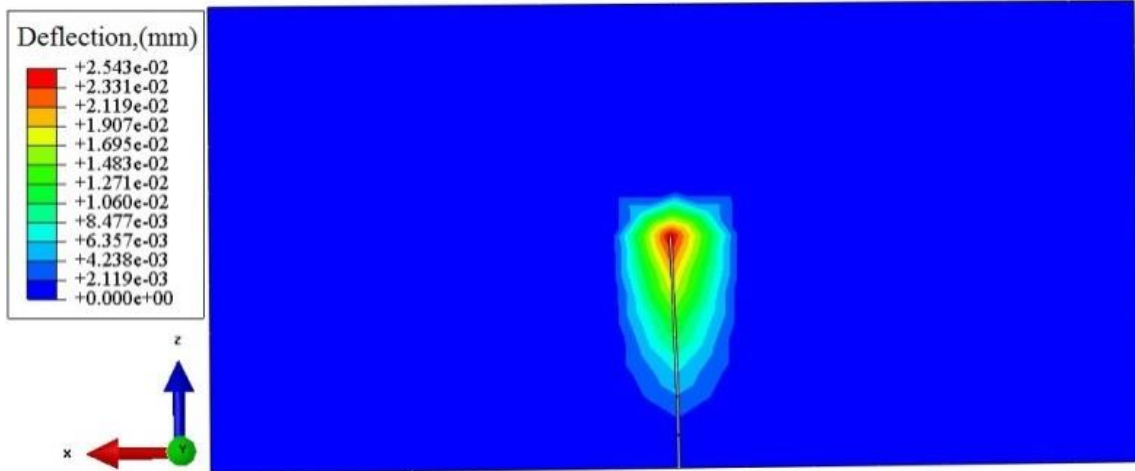


Figure 26: Deflection contour plot of the flexible hair receptor at the time of 0.75 seconds in steady flow

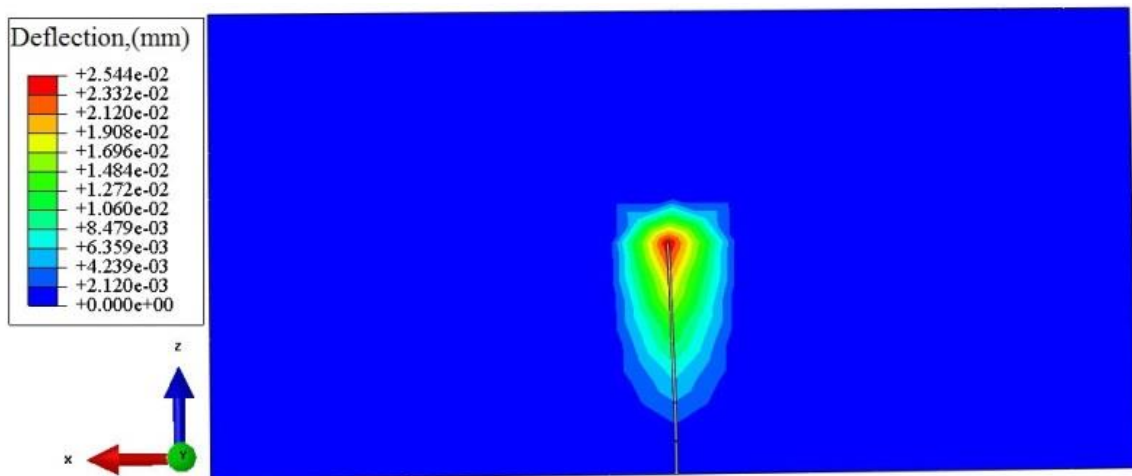


Figure 27: Deflection contour plot of the flexible hair receptor at the time of 1.0 seconds in steady flow

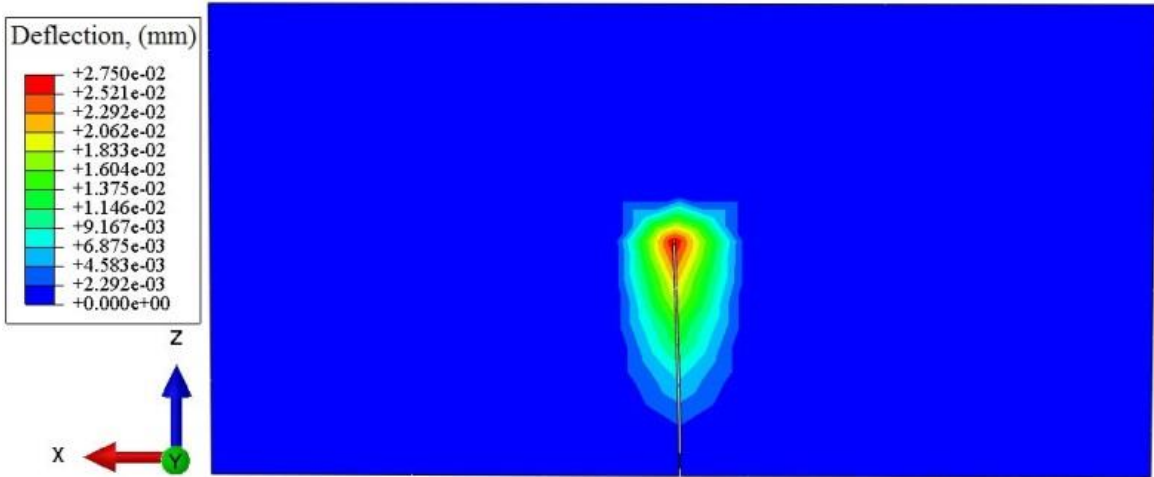


Figure 28: Deflection contour plot of the flexible hair receptor at the time of 0.25 seconds in unsteady flow

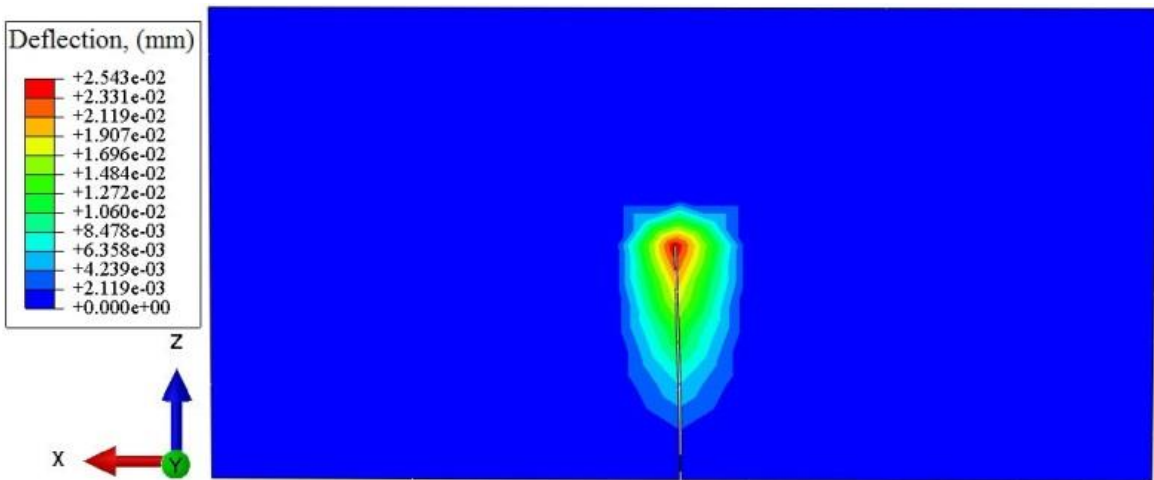


Figure 29: Deflection contour plot of the flexible hair receptor at the time of 0.50 seconds in unsteady flow

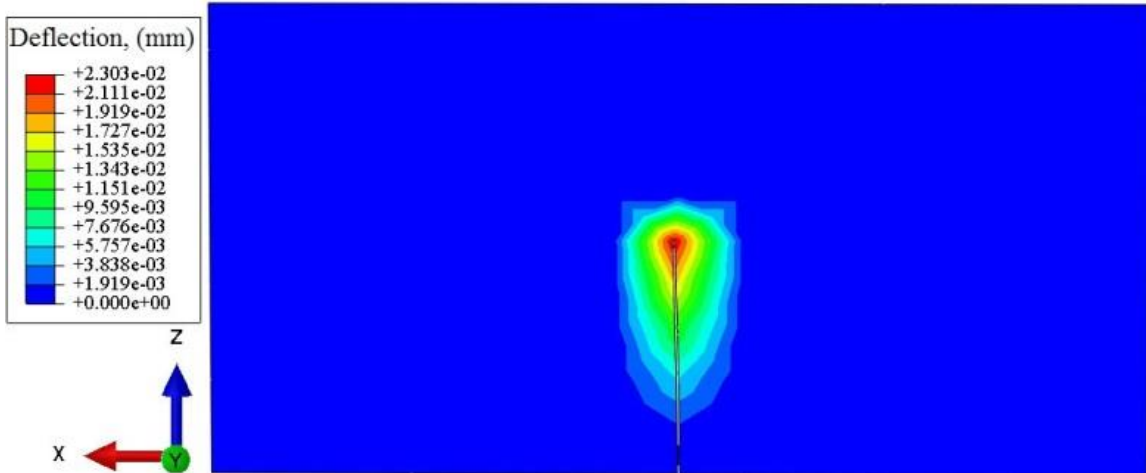


Figure 30: Deflection contour plot of the flexible hair receptor at the time of 0.75 seconds in unsteady flow

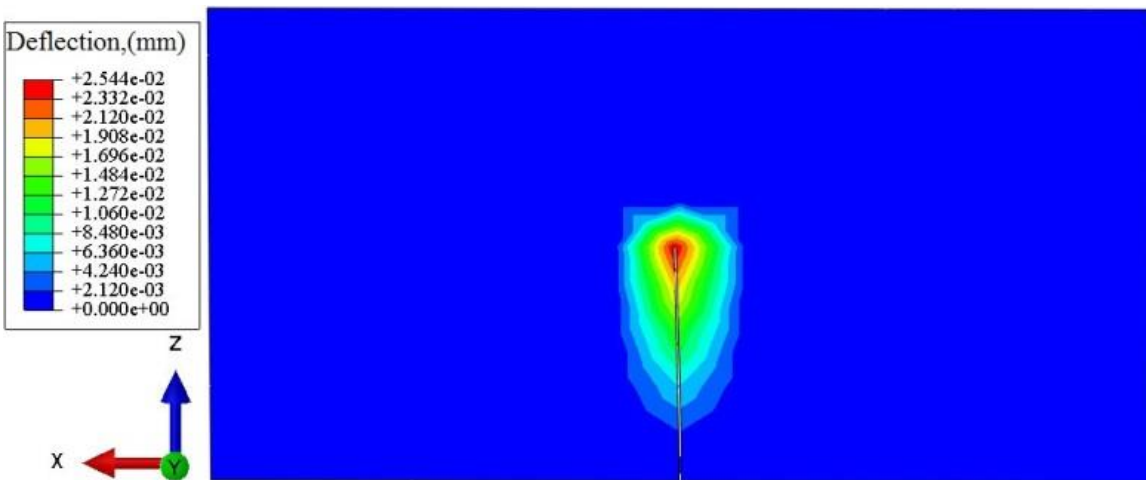


Figure 31: Deflection contour plot of the flexible hair receptor at the time of 1.0 seconds in unsteady flow

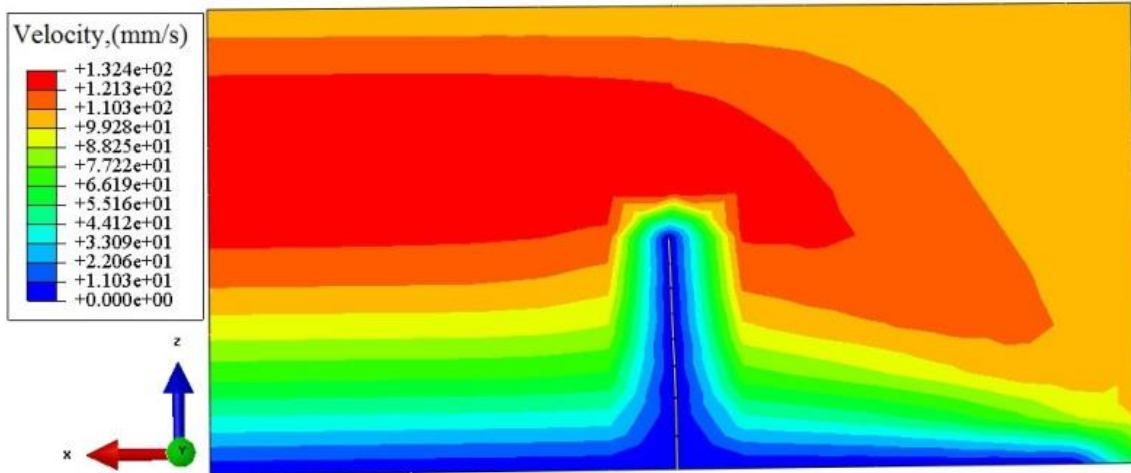


Figure 32: Velocity contour plot of the flexible hair receptor at the time of 1.0 seconds in steady flow

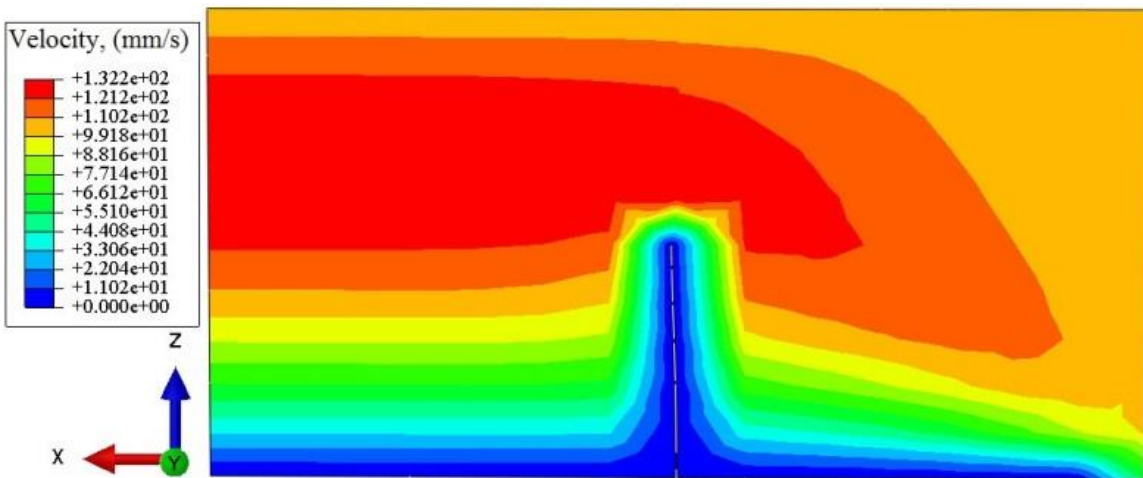


Figure 33: Velocity contour plot of the flexible hair receptor at the time of 1.0 seconds in unsteady flow

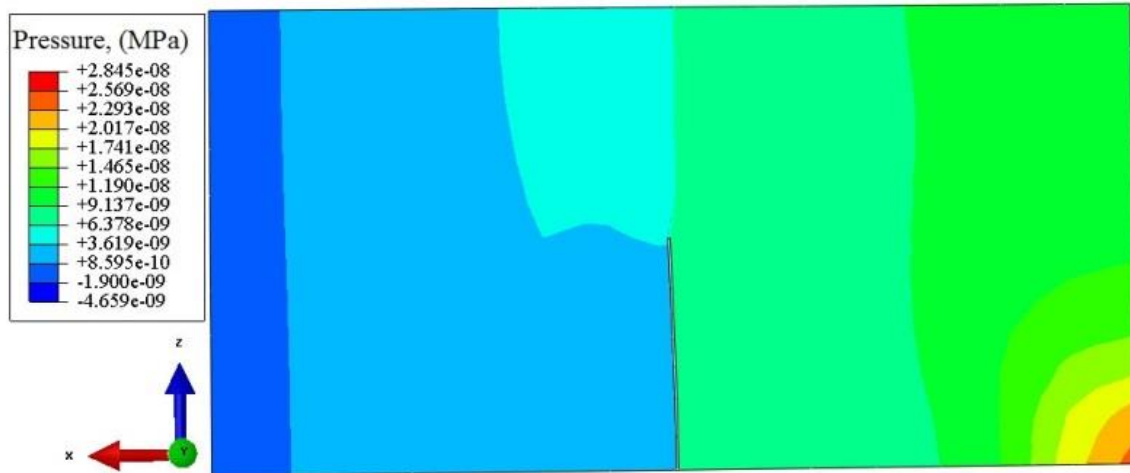


Figure 34: Pressure contour plot of the flexible hair receptor at the time of 1.0 seconds in steady flow

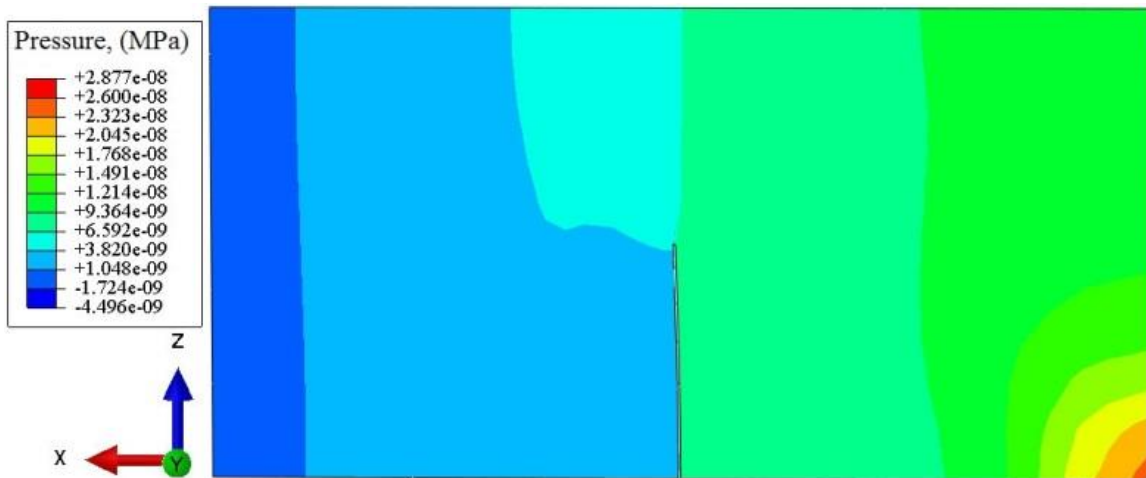


Figure 35: Pressure contour plot of the flexible hair receptor at the time of 1.0 seconds in unsteady flow

5.2. Multiple Hair Receptors Study

One of the objectives of this study is to understand the effect of a hair on its neighbor in terms of tip deflections and bending moment at the base due to the interactions of the surrounding fluid. In particular, the boundary layer development over the flat surface, pressure variations, and the hair tip deflections associated to the flow are very clear to see. Therefore, the approach using MEMS allows us to use the predictions obtained using computational dynamics models and to predict the expected effects for natural hairs, taking into account the similarities and differences between these artificial hairs and natural hairs.

Multiple hair receptors model is evaluated for six hairs with lengths of 1.0 mm and the diameters of 0.01 mm each. Freestream velocity is considered as 0.1 m/s to keep the flow within the creeping flow region is similar to the single hair model. To be consistent with the single hair model, front hair receptors are placed at 2.0 mm from the leading edge of a flat plate. Several runs are conducted to investigate the approximate distances between the hairs to understand the effects of them on its neighbors. At a distances of 1.5 mm or higher, the effect of a hair on its neighbor, in terms of tip deflections, becomes negligible. Therefore, in the present study, the distance between the hairs is considered as 1.0 mm.

The results for the multiple hair receptors model given by the FSI analysis are considered at the vertical mid plane ($x = 0.0$ mm, $y = 0.0$ mm, and $z = 1.0$ mm). The dynamic implicit method is used to perform the structural analysis of six hair receptors. In the steady flow, deflections of the front hair receptors are higher than that of rear ones. The deflection magnitude of the front hair receptor is found to be 0.0202482 mm whereas the deflection magnitude of the rear hair receptors is found to be 0.0201018 mm. Since the hair deflection magnitudes are

proportional to fluid velocity, higher deflections are occurred at the increased fluid flow. This is due to the effect of the fluid velocity perturbed from the neighbor hair.

The deflection contour plot of the hair receptors in the steady flow is shown in Fig. 36. The flow pattern over hair receptors in the steady flow is shown in Fig. 37. The boundary layer developed as the fluid flows over the flat plate. The velocity magnitudes of the fluid adjacent to the plate and the hair receptors are zero. The pressure distribution around the hair receptors in the steady flow is shown in Fig. 38. The pressure values are higher at the front of the hair receptors which represents the stagnation pressure and are lower at the back of the hair receptors which indicates the wake region. As the distance increases in the flow direction, pressure values decrease.

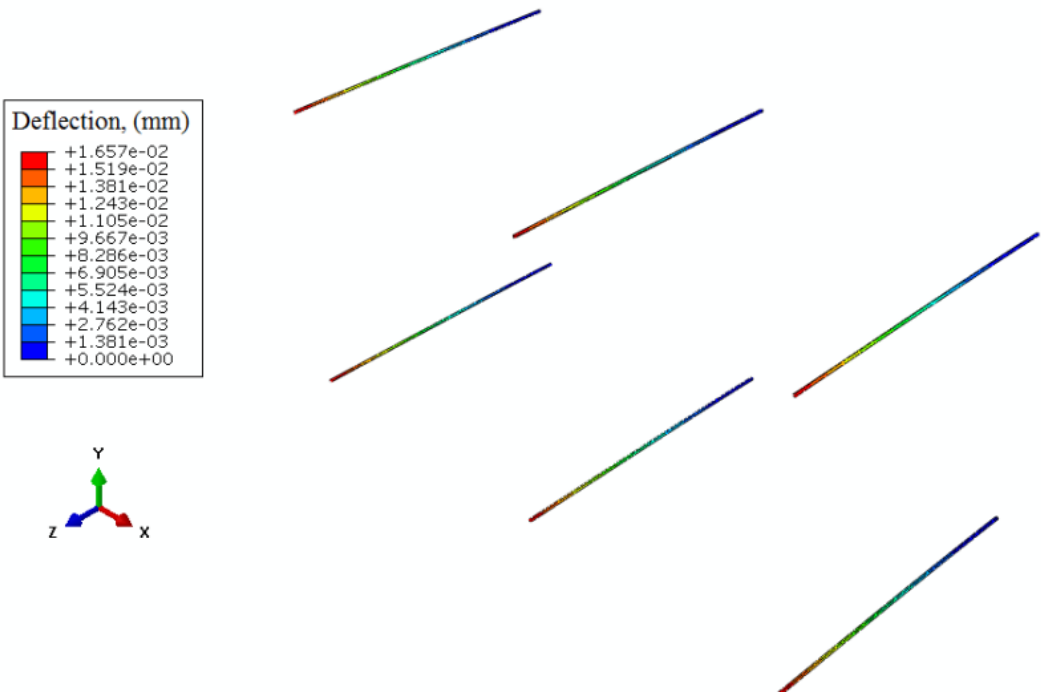


Figure 36: Deflection contour plot of the multiple hair receptors in steady flow

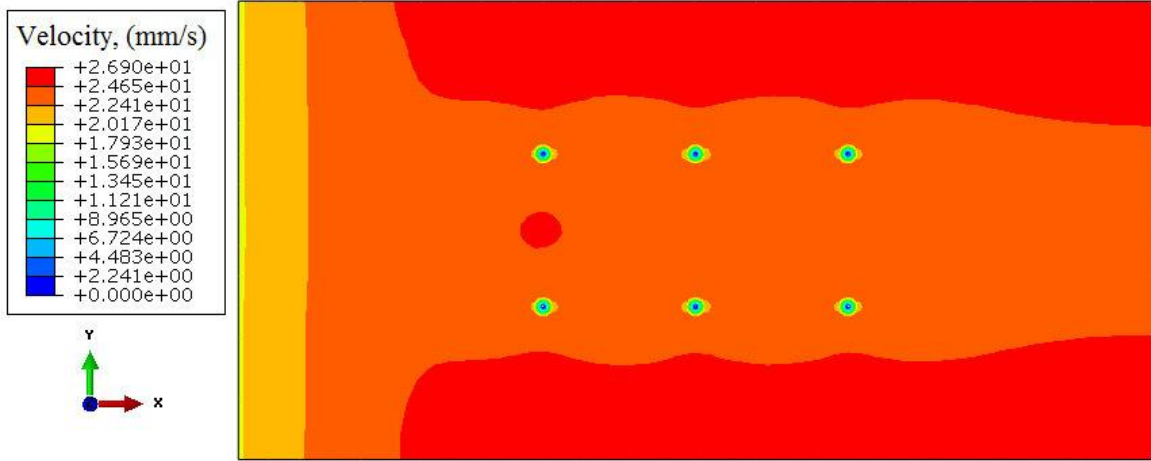


Figure 37: Velocity contour plot of the multiple hair receptors in steady flow

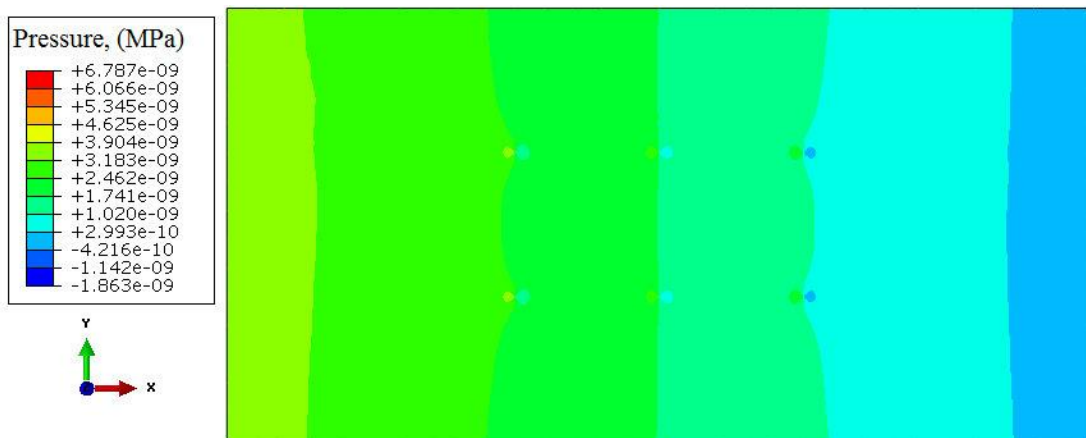


Figure 38: Pressure contour plot of the multiple hair receptors in steady flow

Chapter 6

Conclusions

The dynamic responses of both single hair receptor and multiple hair receptors are studied in terms of the tip deflection and velocity in creeping flow environment. The mode shapes and natural frequencies of the hair receptor in a vacuum are calculated from finite element analysis. Also, the natural frequencies are evaluated from the analytical solution for free vibration and compared with that from finite element analysis. In order to perform this study, a three-dimensional fluid-structure interaction (FSI) model is developed for flexible hair-structure in the airflow, which couples a FE model with a CFD model. Deflection of the hair receptor at the tip and bending moment at the root are calculated at different freestream velocities within the creeping flow environment.

The following conclusions are drawn from this investigation:

1. Velocity, pressure, and deflection contour plots of the hair receptor are studied with the FSI model in both the steady and unsteady flows
2. The deflection and bending moment of the hair receptor increase with freestream velocity. The total drag force acting on the hair structure increases with the velocity of the flow which is used to calculate the value of the shear stress at the root of the hair receptor. Since the drag force is directly proportional to the square of the velocity, the deflections and bending moment of the hair receptors increase with flow velocity

3. The natural frequencies of the hair receptor in a vacuum from finite element model and that from analytical solution are in good agreement. However, the higher the frequency, the more the deviation (although small in magnitude) between finite element and analytical results. This is due to more vibration occurs at higher modes within a small length of the hair element compared to lower modes. Since the mesh density is same for each mode shape, the deviation between finite element and analytical solution increases
4. The effects of both boundary layer and viscous forces are described from the FSI of the hair receptor. Due to the no-slip boundary condition applied on the bottom surface of the flow domain which acts as a flat plate, velocity of the fluid adhering to the plate becomes zero. The viscous forces retard the motion of the fluid in a thin layer near the bottom surface. The velocity of the fluid increases from zero to its freestream velocities where there are no viscous forces applicable
5. The deflection and velocity near the tip of the hair receptor are uniform for the steady flow but vary periodically due to the harmonic unsteady flow. After reaching the steady state, uniform behavior of the fluid is reflected in the steady flow as it is assigned to inlet velocity and the periodic behavior of the fluid is reflected in the unsteady flow as the sinusoidal amplitude is assigned to the incoming velocity
6. The mesh independence of the CFD model is studied to validate the FSI solution. As grid size is refined, the fluid properties in terms of velocity at the selected points on the fluid domain become very close in their magnitudes which confirms the convergence of the solution

7. The interaction among multiple hair receptors is investigated. Deflection of the front hair receptor is higher than that of the rear hair receptor. The tip deflection is affected by the wake development behind the hair receptors which results low drag forces acted on the rear ones

In the future, the following studies are recommended for this research.

1. Conduct the FSI analysis for an airfoil with artificial hair receptors at different angle of attacks
2. Study the flow behavior of multiple hair receptors by comparing the computational distance between the artificial hair receptors with the physical distance between the bat hair flow receptors
3. Investigate the dynamic response of the hair receptor by considering the effects of vortex shedding formed behind the hair receptor
4. Study the effects of three-dimensional fluid flow over the hair receptor in order to investigate the dynamic characteristics within the creeping flow regime
5. Investigate the dynamic response of the hair receptor outside the creeping flow assumption to extend the applicability of wider range of low-Reynolds number platforms

References

- [1] Sterbing-D'Angelo, S., Chadha, M., Chiu, C., Falk, B., Xien, W., Barcelo, J., Zook, J.M., and Moss, C.F., "Bat wing sensors support flight control," *Proceedings of National Academy of Sciences of the United States of America*, Vol. 108, pp. 11291:1–6, 2011
- [2] Dickinson, B.T., Singler, J.R., and Batten, B.A., "Modeling of bioinspired sensors for flow separation detection for micro air vehicles," *Proceedings of the 3rd AIAA Flow Control Conference*, Paper No. 3019, San Francisco, CA, USA, 2006
- [3] Coombs, S., "Smart skins: information processing by lateral line flow sensors," *Autonomous Robots*, Vol. 11, pp. 255–61, 2001
- [4] Liu, C., "Micro-machined biomimetic artificial hair cell sensors," *Bioinspirations and Biomimetics*, Vol. 2, pp. 162–169, 2007
- [5] Abdulrahim, M., Garcia, H., and Lind, R., "Flight characteristics of shaping the wing membrane of a micro air vehicle," *Journal of Aircraft*, Vol. 42, pp. 131–137, 2005
- [6] Stroble, J.K., Stone, R.B., Watkins, S.E., "An overview of biomimetic sensor technology," *Sensor Review*, Vol. 29 (2), pp. 112–119, 2009
- [7] Zook, J.M., "The neuroethology of touch in bats: cutaneous receptors of the wing," *Neuroscience Abstracts*, Vol. 78, pp. 21, 2005
- [8] Chadha, M., and Moss, C., Sterbing-D'Angelo, S., "Organization of the primary somatosensory cortex and wing representation in the big brown bat, *Eptesicus fuscus*," *Journal of Comparative Physiology A, Neuroethology, Sensory, Neural, and Behavioral Physiology*, Vol. 197 (1), pp. 89–96, 2011
- [9] Dickinson, B.T., Singler, J.R., and Batten, B.A., "The detection of unsteady flow separation with bioinspired hair-cell sensors," *Proceedings of the 26th AIAA Aerodynamic Measurement and Ground Testing Conference*, Paper No. 3937, Seattle, WA, USA, 2008
- [10] Dickinson, B., "Detecting fluid flows with bioinspired hair sensors," *PhD Thesis*, Oregon State University, Corvallis, OR, USA, 2009
- [11] Joshi, K., Mian, A., and Miller, J., "Model development and analysis of a cricket filiform hair socket," *Proceedings of the ASME 2012 International Mechanical Engineering Congress & Exposition*, Paper No. 85436, Houston, TX, USA, 2012
- [12] Humphrey, J.A.C., Devarakonda, R., Iglesias, I., and Barth, F.G., "Dynamics of arthropod filiform hairs. 1. Mathematical modeling of the hair and air motions," *Philosophical Transactions of Royal Society B*, Vol. 340 (1294), pp. 423–444, 1993

- [13] Tao, J., and Yu, X., “Hair flow sensors: From bio-inspiration to bio-mimicking – A review,” *Smart Materials and Structures*, Vol. 21, pp. 11300:1–10, 2012
- [14] Maschmann, M.R., Dickinson, B.T., Ehlert, G.T., and Baur, J.W., “Force sensitive carbon nanotube arrays for biologically inspired airflow sensing,” *Smart Materials and Structures*, Vol. 21 (9), pp. 094024:1–10, 2012
- [15] Yu, X., Tao, J., and Berilla, J., “A bio-inspired flow sensor,” *Proceedings of the SPIE*, Vol. 7646, pp. 764618:1–10, 2010
- [16] Chen, N.N., Tucker, C., Engel, J.M., Yang, Y.C., Pandya, S., and Liu, C., “Design and characterization of artificial hair cell sensor for flow sensing with ultrahigh velocity and angular sensitivity,” *Journal of Microelectromechanical Systems*, Vol. 16 (5), pp. 999–1014, 2007
- [17] Tucker, C., Chen, N., Engel, J., Yang, Y., Pandya, S., and Liu, C., “High-sensitivity bi-directional flow sensor based on biological inspiration of animal hair cell sensors,” *5th IEEE Conference on Sensors*, Daegu, Korea, pp. 1440–1442, 2006
- [18] Moliki, M., and Breuer, K., “Oscillatory motions of a prestrained compliant membrane caused by fluid-membrane interaction,” *Journal of Fluids and Structures*, Vol. 26 (3), pp. 339–358, 2010
- [19] Rojratsirikul, P., Wang, Z., and Gursul, I., “Effect of pre-strain and excess length on unsteady fluid-structure interactions of membrane airfoil,” *Journal of Fluids and Structures*, Vol. 26 (3), pp. 359–376, 2010
- [20] Miao, J., and Ho, M., “Effect of flexure on aerodynamic propulsive efficiency of flapping flexible airfoil,” *Journal of Fluids and Structures*, Vol. 22 (3), pp. 401–419, 2006
- [21] Mueller, T., and DeLaurier, J., “Aerodynamics of small vehicles,” *Annual Review of Fluid Mechanics*, Vol. 35, pp. 89–111, 2005
- [22] Mangalam, A., and Moes, T., “Real-time unsteady loads measurements using hot-film sensors,” *International 22nd Applied Aerodynamic conference and Exhibit*, 2004
- [23] Lee, J.S., and Lee, S.W., “Flow around a flexible plate in a freestream,” *Journal of Mechanical Science and Technology*, Vol. 25 (2), pp. 379–390, 2011
- [24] Cummins, B., Gedeon, T., Klapper, I., and Cortez, R., “Interaction between arthropod filiform hairs in a fluid environment”, *Journal of Theoretical Biology*, Vol. 247, pp. 266–280, 2007
- [25] Heys, J.J., Gedeon, T., Knott, B.C., Kim, Y., “Modeling arthropod filiform hair motion using the penalty immersed boundary method,” *Journal of Biomechanics*, Vol. 41, pp. 977–984, 2008

- [26] Kim, S., Nam, T., and Park, S., “Measurement of flow direction and velocity using a micro-machined flow sensor,” *Sensors and Actuators A*, Vol. 114, pp. 312–318, 2004
- [27] Su, Y., Evans, A.G.R., Brunnschweile, A., and Ensell, G., “Characterization of a highly sensitive ultrathin piezoresistive silicon cantilever probe and its application in gas flow velocity sensing,” *Journal of Micromechanics and Microengineering*, Vol. 12, pp. 780–785, 2002
- [28] Necker, R., “Receptors in the wing of the pigeon and their possible role in bird flight,” *Biona Rep 3: Vogelflug, ed Nachtigall W (Fischer, Stuttgart)*, pp. 433–444, 1985
- [29] Haskell, P.T., “Physiology of some wind-sensitive receptors of the desert locust,” (Schistocerca gregaria). *XVth International Zool Congress (London)*, pp. 960–961, 1958
- [30] Pflueger, H.J., and Tautz, J., “Air movement sensitive hairs and interneurons in *Locusta migratoria*,” *Journal of Comparative Physiology A, Neuroethology, Sensory, Neural, Behavioral, Physiology*, Vol. 145, pp. 369–380, 1982
- [31] Dijkstra, M., Van Baar, J.J., Wiegerink, R.J., Lammerink, T.S.J., De Boer, J.H., and Krijnen, G.J.M., “Artificial sensory hairs based on the flow sensitive receptor hairs of crickets,” *Journal of Micromechanics and Microengineering*, Vol. 15, pp. 132–138, 2005
- [32] Dickinson, B.T., “Hair receptor sensitivity changes in laminar boundary layer shape,” *Bio-Inspirations and Biomimetics*, Vol. 5 (1), pp. 016002:1–11, 2010
- [33] McClain, S.T., Case, L., and Dickinson, B.T., “Response of passive surface hairs in steady boundary layers,” *6th AIAA Flow Control Conference*, Paper No. 3047, New Orleans, LA, USA, 2012
- [34] Emine, K., Eugenio, A., Akif, I., and Padmanabhan, S., “A stability estimate for fluid-structure interaction problem with non-linear beam,” *Discrete and Continuous Dynamical Systems*, pp. 424–434, 2009
- [35] Dickinson, B.T., Singler, J.R., and Batten, B.A., “Mathematical modeling and simulation of biologically inspired hair receptor arrays in laminar unsteady flow separation,” *Journal of Fluids and Structures*, Vol. 29, pp. 1–17, 2012
- [36] Weiss, B., Reichel, E. K., Jakoby, B., 2008. “Modeling of a clamped-clamped beam vibrating in a fluid for viscosity and density sensing regarding compressibility,” *Sensors and Actuators A: Physical*, Vol. 143 (2), pp. 293–301, 2008
- [37] Tuck, E. O., “Calculation of unsteady flows due to small motions of cylinders in a viscous fluid,” *Journal of Engineering Mathematics*, Vol. 3 (1), pp. 29–44, 1969
- [38] Shimozawa, T., Kumagai, T., and Baba, Y., “Structural scaling and functional design of the cercal wind-receptor hairs of cricket,” *Journal of Comparative Physiology A*, Vol. 183, pp. 171–186, 1998

- [39] Dechant, H.E., Rammerstrofer, F.G., and Barth, F.G., “Arthropod touch reception: stimulus transformation and finite element model of spider tactile hairs,” *Journal of Comparative Physiology A*, Vol. 187, pp. 313–322, 2001
- [40] Henson, B.L., and Wilkins, L.A., “A mathematical model for the motion of mechanoreceptor hairs in fluid environments,” *Journal of Biophysics*, Vol. 27, pp. 277–286, 1979
- [41] Shimozawa, T., and Kanou, M., “The aerodynamics and sensory physiology of range fractionation in the cercal filiform sensilla of the cricket *Gryllus bimaculatus*,” *Journal of Comparative Physiology A*, Vol. 155, pp. 495–505, 1984
- [42] Humphrey, J.A.C., Barth, F.G., Reed, M. and Spak, A., “The physics of arthropod medium-flow sensitive hairs: biological models for artificial sensors,” *Sensors and Sensing in Biology and Engineering*, Springer Verlag, pp. 129–144, 2003
- [43] Byung, K.P., and Joon, S.L., “Dynamic behavior of flexible sensory hair in an oscillating flow,” *Journal of Mechanical Science and Technology*, Vol. 26 (4), pp. 1275–1282, 2012
- [44] Hossain, A., and Mian, A., “Characterize dynamic response of cantilevers submerged in viscous fluids,” *Proceedings of the ASME 2012 International Mechanical Engineering Congress & Exposition*, Paper No. 85096, Houston, TX, USA, 2012
- [45] Steinmann, T., Casas, J., Krijnen, G., and Dangles, O., “Air-flow sensitive hairs: boundary layers in oscillatory flows around arthropod appendages,” *Journal of Experimental Biology*, Vol. 209, pp. 4398–4408, 2006
- [46] Devarakonda, R., Barth, F.G., and Humphrey, J.A.C., “Dynamics of arthropod filiform hairs. iv. Hair motion in air and water,” *Philosophical Transactions: Biological Sciences*, Vol. 351, pp. 933–946, 1996
- [47] Dickinson, B.T., McClain, S.T., and Case, L., “The dynamic response of quasi-steady hair-like structures in oscillatory boundary layer flows,” *6th AIAA Flow Control Conference*, Paper No. 3048, New Orleans, LA, USA, 2012
- [48] Cao, D., Dongsheng, L., Charles, H., and Wang, T., “Nonlinear dynamic modeling for mems components via the cosserat rod element approach,” *Journal of Micromechanics and Microengineering*, Vol. 15, pp. 1334–1343, 2005
- [49] Cao, D., Dongsheng, L., Charles, H., and Wang, T., “Three dimensional nonlinear dynamics of slender structures: Cosserat rod element approach,” *International Journal of Solids and Structures*, Vol. 43, pp. 760–783, 2006
- [50] Bathe, K., “Conserving energy and momentum in nonlinear dynamics: A simple implicit time integration scheme,” *Computers and Structures*, Vol. 85, pp. 437–445, 2007

- [51] Badiane, D., Gasser, A., and Blond, E., “Vibrating beam in viscous fluid for viscosity sensing: Application to an industrial vibrating viscometer.” *Proceedings of 12th Pan-American Congress of Applied Mechanics - PACAM XII*, Port of Spain, Trinidad, 2012
- [52] Wagner, H., and Ramamurti, V., “Beam vibrations- A review,” *The Shock and Vibration Digest*, Vol. 9, pp. 17–24, 1977
- [53] Reddy, J.N. “Finite element modeling of structural vibrations: A review of recent advances,” *The Shock Vibration Digest*, Vol. 11, pp. 25–39, 1990
- [54] Evensen, D.A., “Nonlinear vibrations of beams with various boundary conditions,” *AIAA Journal*, Vol. 6, pp. 370–372, 1968
- [55] Lou, C.L. and Sikarskie, D.L., “Nonlinear Vibration of beams using a form-function approximation,” *ASME Journal of Applied Mechanics*, Vol. 42, pp. 209–214, 1975
- [56] Mei, C., “Finite element displacement method for large amplitude free flexural vibrations of beams and plates,” *Computers and Structures*, Vol. 3, pp. 163–174, 1973
- [57] Singh, G., Rao, G.V., and Iyengar, N.G.R., “Reinvestigation of large amplitude free vibrations of beams using finite elements,” *Journal of Sound and Vibration*, Vol. 143, pp. 351–355, 1990
- [58] Evensen, D.A., “Nonlinear vibrations of beam with various boundary conditions”, *AIAA Journal*, Vol. 6 (2), pp. 370–372, 1968
- [59] Lee, J.H., Lee, S. T., Yao, C. M., and Fang, W., “Comments on the size effect on the micro-cantilever quality factor in free air space,” *Journal of Micro Mechanics and Micro Engineering*, Vol. 17, pp. 139–146, 2007
- [60] Basak, S., and Raman, A., “Hydrodynamic loading of micro-cantilevers vibrating in viscous fluids,” *Journal of Applied Physics*, Vol. 99 (11), pp. 114906:1–10, 2006
- [61] Ricci, A., and Giuri, E. “FSI analysis of micro-cantilevers vibrating in fluid environment,” *Proceedings of the COMSOL Conference*, Milan, 2009
- [62] Da Lozzo, E., Auricchio, F., and Calvi, G.M., “Added mass model for vertical circular cylinder partially immersed in water,” *Proceedings of the 15th World Conference on Earthquake Engineering*, Lisbon, Portugal, 2012
- [63] Sader, J. E., “Frequency response of cantilever beams immersed in viscous fluids with applications to the atomic force microscope,” *Journal of Applied Physics*, Vol. 84 (1), pp. 64–76, 1998
- [64] Van Eysden, C. A., and Sader, J. E., “Resonant frequencies of a rectangular cantilever beam immersed in a fluid,” *Journal of Applied Physics*, Vol. 100 (11), pp. 114916:1–8, 2006

- [65] Elmer, F. J., and Dreier, M. "Eigen frequencies of a rectangular atomic force microscope cantilever in a medium," *Journal of Applied Physics*, Vol. 81 (12), pp. 7709–7714, 1997
- [66] Holtsmark, J., Johnsen, I., Sikkeland, T., and Skavlem, S., "Boundary layer flow near a cylindrical obstacle in an oscillating, incompressible fluid," *The Journal of the Acoustical Society of America*, Vol. 26, pp. 26–39, 1954
- [67] Dowell, E.H., and Hall, K.C., "Modeling of fluid-structure interaction." *Annual Review of Fluid Mechanics*, Vol. 33, pp. 445–490, 2001
- [68] Zhang, W., Requa, M., and Turner, K., "Determination of frequency dependent fluid damping of micro and nano resonators for different cross-sections," *Nanotechnology 2006*, Vol. 1, pp. 721–724, 2006
- [69] Zhang, W., and Turner, K., "Frequency dependent fluid damping of micro/nano flexural resonators: Experiment, model and analysis," *Sensors and Actuators A*, Vol. 134, pp. 594–599, 2007
- [70] Rezazadeh, G., Fathalilou, M., and Shabani, R., "Dynamic characteristics and forced response of an electrostatically-actuated microbeam subjected fluid loading," *Journal of Microsystems Technology*, Vol. 15, pp. 1355–1363, 2007
- [71] Lucey, A.D., and Carpenter, P.W., "The Hydrostatic stability of three-dimensional disturbances of finite compliant wall," *Journal of Sound and Vibration*, Vol. 165 (3), pp. 527–552, 1992
- [72] Wang, X.Q., So, R.M.C., and Liu, Y., "Flow-induced vibration of an Euler-Bernoulli beam," *Journal of Sound and Vibration*, Vol. 243, pp. 241–268, 2001
- [73] Houston, B.H., Martin, M.J., and Fathy, H.K., "Dynamic simulation of atomic force microscope cantilevers oscillating in liquid," *Journal of Applied Physics*, Vol. 104 (4), pp. 044316:1–8, 2008
- [74] Borges, A.S., Vedovoto, J.M., Mariano, F.P., Da Silveira Neto, A., and Rade, D.A., "Fluid-structure interaction of cylinders by combining the cosserat beams theory and immersed boundary methodology," *The Argentine Association for Computational Mechanics*, Vol. 29, pp. 3237–3255, 2010
- [75] Cesur, A., and Feymark, A., "Fluid-structure interaction of the transient evolution of a cantilever beam," *Proceedings of the 25th Nordic Seminar on Computational Mechanics*, pp. 49–52, 2012
- [76] Vashist S. K., "A review of microcantilevers for sensing applications", *Journal of Nanotechnology*, Vol. 3, 2007

- [77] Krijnen, G., Dijkstra, M., Van Baar, J., Shankar, S., Kuipers, W., de Boer R., Altpeter, D., Lammerink, T., and Wiegering, R., "MEMS based hair flow-sensors as model systems for acoustic perception studies," *Nanotechnology*, Vol. 17, pp. S84–S89, 2006
- [78] Ozaki, Y. Ohyama, T. Yasuda, T., and Shimoyama, I., "Air flow sensor modeled on wind receptor hairs of insects," *Proceedings of IEEE International Conference MEMS*, Miyazaki, pp. 531–536, 2000
- [79] Van Baar, J.J., Dijkstra, M., Wiegerink, R., Lammerink, T.S.J. de Boer, R., and Krijnen, G.J.M., "Arrays of cricket-inspired sensory hairs with capacitive motion detection", *Proceedings of IEEE International Conference MEMS*, Miami, pp. 646–649, 2005
- [80] Kuipers, W.J., Van Baar, J.J., Dijkstra, M., Wiegerink, R.J., Lammerink, T.S.J. de Boer, J.H., Krijnen, G.J.M., "Drag force actuated bistable microswitches for flow sensing," *Proceedings of IEEE International Conference MEMS*, pp. 658–661, 2006
- [81] Bruinink, C.M., Jaganatharaja, R.K., de Boer, M.J., Berenschot, E., Kolster, M.L., Lammerink, T.S.J., Wiegerink, R.J. and Krijnen, G.J.M., "Advancements in technology and design of biomimetic flow-sensor arrays," *Proceedings of IEEE International Conference MEMS*, pp. 152–155, 2009
- [82] Casas, J., Steinmann, T., and Krijnen, G., "Why do insects have such a high density of flow-sensing hairs? Insights from the hydromechanics of biomimetic MEMS sensors," *Journal of Royal Society Interface*, Vol. 7 (51), pp. 1487–1495, 2010
- [83] Lewin, G.C., and Hallam, J., "A computational fluid dynamics model of viscous coupling of hairs," *Journal of Comparative Physiology A*, Vol. 196 (6), pp. 385–395, 2010
- [84] Fu Y., Price W.G., "Interactions between a partially or totally immersed vibrating cantilever plate and the surrounding fluid", *Journal of Sound and Vibration*, Vol. 118 (3), pp. 495–513, 1987
- [85] Gere, J.M., and Goodno, B.J., *Mechanics of Materials (Brief Edition)*, Cengage Learning, USA, 2012
- [86] Voltera, E., Zachmanoglou, E.C., *Dynamics of Vibrations*, Charles E, Merrill Book, Inc., Columbus, USA. 1965
- [87] Atkins, P.W. *Physical Chemistry*, W.H. Freeman and Company, 5th Edition, New York, USA, 1994
- [88] Abaqus, Software Package, Version 6.12, SIMULIA, Providence, RI, USA, 2012
- [89] Chidurala, M., Dickinson, B.T., and Chakravarty, U.K., "Dynamic response of biomimetic hair receptors in both steady and unsteady flow environment," *Proceedings of the ASME 2013*

International Mechanical Engineering Congress & Exposition, Paper No. 65250, San Diego, California, USA, 2013

[90] Paulo, A.B. de Sampaio, Patricia, H. Hallak, Alvaro, L.G.A.Coutinho, and Michele, S. Pfeil, “A stabilized finite element procedure for turbulent fluid-structure interaction using adaptive time-space refinement,” *International Journal for Numerical Methods in Fluids*, Vol. 44, pp. 673–693, 2004

[91] Den Hartog, J. P., *Mechanical Vibrations*, Dover Publications.com, 1956

[92] Kundu, P., and Cohen, I., *Fluid Mechanics*, Elsevier Science, 2010

[93] Inman, D.J., *Engineering Vibration*, Pearson Education Inc., New Jersey, USA, 2007

[94] Park, C.W., and Lee, S.J., “Flow structure around a finite circular cylinder embedded in various atmospheric boundary layers,” *Fluid Dynamic Research*, Vol. 30, pp. 197–215, 2002

Vita

The author was born in Warangal, India. He obtained his Bachelor's degree in Mechanical Engineering from Jawaharlal Nehru Technological University College of Engineering (Autonomous) in 2006. He started his graduate studies at the University of New Orleans in 2007 and received his Master of Science in Mechanical Engineering degree in 2009. He then continued his graduate studies at the University of New Orleans from 2010 to pursue a Ph.D. in Engineering and Applied Sciences.